J. Fluid Mech. (2025), *vol.* 1025, A48, doi:10.1017/jfm.2025.10943

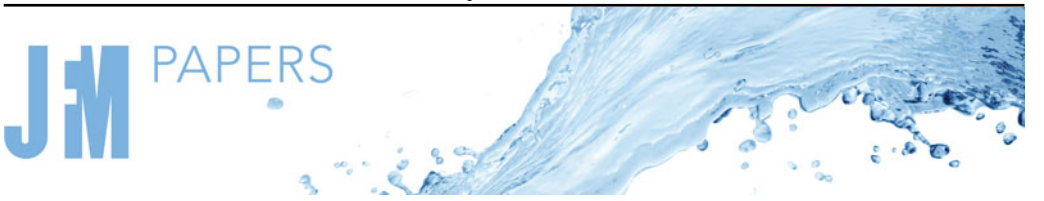

Instabilities in the flow over a spinning disk at angle of attack

Marcus Kuok Kuan Lee[1,†], **Tim Colonius**[1] **and Beverley J. McKeon**[2,‡]

[1]Department of Mechanical and Civil Engineering, California Institute of Technology, Pasadena, CA 91125, USA

[2]Graduate Aerospace Laboratories, California Institute of Technology, Pasadena, CA 91125, USA

Corresponding author: Marcus Kuok Kuan Lee, mlee406@ucmerced.edu

(Received 17 April 2025; revised 19 September 2025; accepted 6 November 2025)

Three-dimensional laminar flow over an inclined spinning disk is investigated at a Reynolds number of $Re = 500$ and an angle of attack of $\alpha = 25°$, for tip-speed ratios up to 3. Numerical simulations are performed to investigate the effect of spin on the aerodynamics and characterise the instabilities that occur. Increasing tip-speed ratio significantly increases both lift and drag monotonically. Several distinct wake regimes are observed, including vortex shedding in the non-spinning case, vortex-shedding suppression at moderate tip-speed ratios and a distinct corkscrew-like short-wavelength instability in the advancing tip vortex at higher tip-speed ratios. Vorticity generated by the spinning disk strengthens the advancing tip vortex, inducing a spanwise stretching in the trailing-edge vortex sheet. This helps to dissipate the vorticity, which in turn prevents roll up and suppresses vortex shedding. The short-wavelength instability shows qualitative and quantitative matches to the $(-2, 0, 1)$ principal mode of the elliptic instabilities seen in pairs of counter-rotating Batchelor vortices. The addition of vorticity from the disk rotation significantly alters the circulation and axial velocity in the tip vortices, giving rise to elliptic instability despite its absence in the non-spinning case. In select cases, lock-in between the frequency of the elliptic instability and twice the spin frequency is observed, indicating that disk rotation acts as an additional forcing for the elliptic instability. Additional simulations at different Reynolds numbers and angle of attacks are considered to examine the robustness of observed phenomena across different parameter combinations.

Key words: vortex shedding, wakes, bifurcation

[†] *Current address*: Department of Mechanical and Aerospace Engineering, University of California Merced, Merced, CA 95343, USA.

[‡] *Current address*: Department of Mechanical Engineering, Stanford University, Stanford, CA 94305, USA.

1. Introduction

Micro air vehicles (MAVs) face stability issues in the presence of gusty winds, especially as their size is scaled down (Pines & Bohorquez 2006). Several authors have studied spinning-disk flight and suggested its application to MAV design (Stilley & Carstens 1972; Potts & Crowther 2002; Lorenz 2007). An example of a spinning disk is the recreational Frisbee, which leverages spin-stabilisation to achieve robust flight in the presence of environmental disturbances (Potts & Crowther 2002). In addition to the spin dynamics, a spinning disk in an otherwise quiescent fluid rotates and propels fluid outward near the disk surface, drawing in fluid towards the disk surface from above, creating a swirling flow towards the disk (von Kármán 1921). The ability of the rotating disk to inject both linear and angular momentum into the flow with a net-zero mass flux has applications in flow control. Wall-flush-mounted rotating disks (Ricco & Hahn 2013) and rotating rings (Olivucci, Ricco & Aghdam 2019) can reduce drag by up to 20 % in turbulent channel-flow configurations. Similarly, Munday & Taira (2018) used swirling jets, which also inject linear and angular momentum into the flow, to reduce drag and suppress flow separation for a turbulent aerofoil. However, applications in flight and flow control require a thorough understanding of the effect that spin has on the spinning-disk aerodynamics, instabilities and wake structures. Therefore, we aim to investigate the effects of rotation for spinning disks at angle of attack, in particular at Reynolds numbers of $O(10^2)$ where the flow first bifurcates.

Ouyang *et al.* (2022) characterised several flow regimes for normal flow at Reynolds numbers of $O(10^2)$ over a streamwise-rotating disk and showed that rotation can significantly impact wake structures and can even suppress vortex shedding. However, the combined effects of rotation and angle of attack at low Reynolds number remain unexplored, perhaps owing to the large parameter space spanned by three main non-dimensional parameters: Reynolds number, $Re = \rho UD/\mu$; angle of attack, α; and tip-speed ratio (TSR), λ, where ρ is the fluid density, U is the free stream velocity, D is the disk diameter and μ is the dynamic viscosity. The TSR, $\lambda = \Omega R/U$, is the ratio between the disk-edge velocity and the free stream velocity, where Ω is the disk angular velocity around its axis of rotational symmetry and R is the disk radius. Further parameters are associated with the disk's cross-section including an aspect ratio $\chi = D/t_d$, where t_d is the thickness, for the case of a rectangular cross-section; camber, for a curved disk (e.g. a Frisbee); and edge shape/rim. We can also define a rotational Reynolds number $Re_\Omega = \rho\Omega RD/\mu = \lambda Re$, which remains defined when $U = 0$. Each of these parameters acts as a bifurcation parameter in the flow, leading to a complex and multi-dimensional space of flow regimes. The flow configuration and parameters are depicted schematically in figure 1.

In this study, we focus on $Re = O(10^2)$, where the flow initially bifurcates. While this regime is not typically reached even for the smallest MAVs, instabilities clearly identified in this regime may persist to high Reynolds number, albeit modulated by further bifurcations and ultimately the emergence of turbulence. Such behaviour is common to many bluff-body and aerodynamic flows, for example, the vortex shedding first occurring in two-dimensional flow over a bluff body at $Re \approx 50$ persists in this way as $Re \to \infty$. In addition, as a canonical flow, a spinning disk at these low Re may be applicable to other applications, for example, as wall-flush-mounted actuators for flow control and drag reduction as already mentioned (Ricco & Hahn 2013; Olivucci *et al.* 2019).

Past studies of spinning-disk flight at angle of attack consist of experimental studies of Frisbee-like geometries with camber and rims, performed at $Re = O(10^5)$ to match typical Frisbee-flight Reynolds numbers. Potts & Crowther (2001, 2002) experimentally investigated spinning-disk flight at $Re = O(10^5)$, $-10° \leq \alpha \leq 30°$ and $0 \leq \lambda \leq 1.04$,

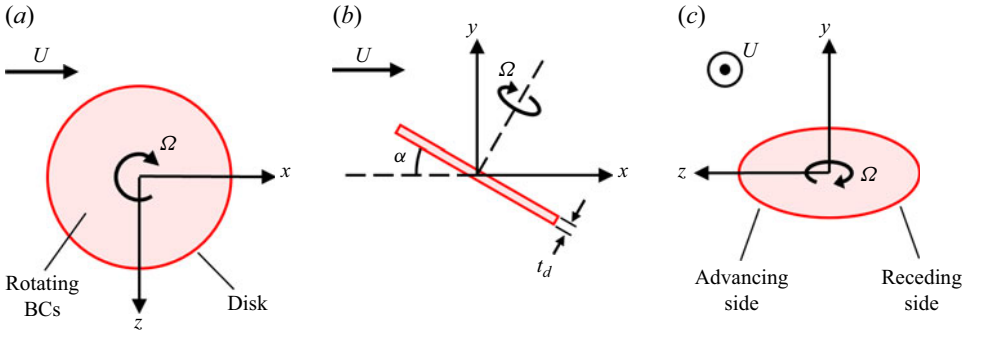

Figure 1. Schematic of set-up for (*a*) top view, (*b*) side view and (*c*) upstream view. The free stream velocity, U, is in the positive x direction.

reporting various aerodynamic and moment coefficient data for a Frisbee-like geometry. Within this parameter range, they found a negligible effect of spin on lift and drag (2001), but found that spin has some effect on pitching moment, rolling moment and side force coefficients (2002). Early studies of thick cylindrical disks ($2 \leq \chi \leq 3$) by Stilley & Carstens (1972) similarly found that for $\lambda < 1$, spin has a negligible effect on lift and drag coefficients. Potts (2005) compared aerodynamic forces and moments for various Frisbee- and discus-like disk geometries. For TSRs above $\lambda = 1$ and up to $\lambda = 3.46$, Potts (2005) found that lift and drag could increase significantly across a broad range of angles of attack from $-10°$ to $30°$ ($\Delta C_L \approx 0.5$ and $\Delta C_D \approx 0.2$). More recently, Kuraan & Savaş (2024) performed smoke-wire visualisation and particle image velocimetry to investigate the near-surface flow structures and boundary layer profile for flow over a $\chi \approx 13.5$ disk with a chamfered edge at a Reynolds number of 2.7×10^4, $54° \leq \alpha \leq 90°$ and $0 \leq \lambda \leq 10$. They observe two vortex-shedding modes that dominate at different angles of attack. They also conclude that the centrifugal forces from the disk spin lead to cross-stream instability with visual similarities to Kelvin–Helmholtz shear layer instability.

Studies of inclined spinning disks have been restricted to high-Reynolds-number flows and have been limited in their ability to examine and visualise flow structures due to the complex, unsteady, three-dimensional (3-D) nature of the flow. As a result, it is still unclear how spin affects the vortical structures and instabilities present in wake, especially those originating as bifurcations at low Reynolds numbers. We turn to the more extensive literature on flow over spinning disks in normal flow ($\alpha = 90°$) and non-spinning, inclined disks to extract some helpful background on some of the expected flow regimes present for the combined spinning and translating disk.

Normal flow ($\alpha = 90°$) over a non-spinning disk has been extensively studied, and the reader is directed to numerical work by Chrust, Bouchet & Dusek (2010) characterising the various initial bifurcations and flow stages at $Re = O(10^2)$, many of which persist for inclined flow. More recent studies by Chrust *et al.* (2015), Tian *et al.* (2017) and Gao *et al.* (2018) have extensively examined bifurcations in flow over the non-spinning, inclined disk as angle of attack is varied. Tian *et al.* (2017) and Gao *et al.* (2018) found that increasing angle of attack and/or Reynolds number leads the flow from steady to chaotic, passing through different stages in the intermediate periodic states depending on the exact parameter configuration. Specifically for $Re = 500$, Tian *et al.* (2017) demonstrated that increasing angle of attack leads to several flow transitions similar to those observed for normal flow, namely: (i) steady planar-symmetric flow; (ii) periodic vortex shedding; (iii) periodic shedding with low-frequency modulation (PSL) and (iv) symmetry-breaking chaotic flow. It is important to note that increasing angle of attack can be either stabilising

or destabilising, depending on the Reynolds number and angle of attack. As a result, the transition through flow stages can be non-monotonic as the angle of attack changes; at certain Reynolds numbers, increasing angle of attack can transition the flow forwards and backwards between flow regimes (Gao *et al.* 2018). In particular, Gao *et al.* (2018) observe a PSL flow regime at moderate angles of attack in the range of $33° \lessapprox \alpha \lessapprox 58°$ for sufficiently high Reynolds numbers in the range of $Re = O(10^2)$, with the transition Reynolds number reaching a minimum of $Re \approx 268$ at $\alpha = 50°$. Gao *et al.* (2018) provide a detailed map of the flow regimes in the Re, α parameter space for the non-spinning disk. The first bifurcation is a Hopf bifurcation that maintains spanwise-planar symmetry and transitions the flow from a steady state to a periodic wake with hairpin-vortex shedding from the trailing edge (Chrust *et al.* 2015). The PSL regime corresponds to a strengthening and weakening of the vortices shed from the disk, reflected in the growing and lessening amplitude of lift and pressure signals. The reader is referred to work by Gao *et al.* (2018), who conducted a thorough Re–α parameter study for $50 \leq Re \leq 300$ and $10° \leq \alpha \leq 90°$, mapping the boundaries between these flow regimes. Chrust *et al.* (2015) also compared the infinitely thin disk ($\chi = \infty$) with a case having a finite thickness ($\chi = 6$) and showed that for high angles of attack ($\alpha \gtrapprox 50°$), increased thickness delays the Hopf bifurcation to higher Reynolds numbers. However, this effect appears to reverse for low angles of attack ($\alpha \lessapprox 40°$), with thicker disks reducing the critical Reynolds number instead (Chrust *et al.* 2015; Gao *et al.* 2018).

While the above-mentioned studies have thoroughly examined the individual effects of either rotation or inclination for Reynolds numbers near the onset of bifurcations, no studies have investigated the combined effects of rotation and inclination at low Reynolds numbers. Given the significant role of rotation in altering wake structures and instability (Kim & Choi 2002; Ouyang *et al.* 2022), this study aims to address this gap by exploring these combined effects. To this end, we perform direct numerical simulations of the spinning disk at angle of attack in regimes that lie at the intersection between available studies on laminar flow over non-spinning disks and on spinning-Frisbee flight in turbulent regimes. We consider TSRs up to $\lambda = 3$, for $Re = 500$ and $\alpha = 25°$ around the first bifurcation from steady flow, and explore the flow regimes that emerge from varying TSR. In § 2, we describe and validate the numerical formulation used to simulate the flow. In § 3, we investigate the changing aerodynamic forces and wake structures with TSR, observing the suppression of vortex-shedding and the emergence of a short-wavelength instability. In § 4, we further explore the stabilising effect of spin on the vortex-shedding instability, and use streamline and vortex line visualisations to understand the underlying mechanism. Finally, we summarise our findings, draw connections with similar rotating bluff-body flows and present ideas for future work in § 5.

2. Computational methodology and set-up

2.1. *Governing equations and numerical method*

To simulate flow over a spinning disk, we use the IBLGF (immersed boundary lattice Green's function) method to solve the 3-D incompressible Navier–Stokes equations on a formally infinite domain (Liska & Colonius 2017). The method uses a standard second-order staggered-mesh finite-volume scheme, which, owing to the unbounded domain, leads to a number of useful commutative properties that, in turn, lead to discrete conservation properties, provable stability and an efficient solution algorithm. The no-slip boundary condition at the immersed boundary (IB) points is enforced implicitly at each step using a projection method. The associated Poisson equation is inverted, using the LGF, to predict

the pressure in a finite, adaptive region defined by a source that is non-zero only where the vorticity is non-zero, which in practice means that it exceeds a certain user-defined threshold value, ϵ. Extensive details on the IBLGF formulation as well as extensive validation for grid resolution, Δx; temporal discretisation, Δt; domain adaption threshold, ϵ; and IB point spacing, Δs, are given by Liska & Colonius (2014, 2016, 2017).

The IBLGF method handles arbitrarily accelerating bodies by using an accelerating reference frame that can translate and rotate with the body. To avoid the prohibitively small time steps required to satisfy Courant–Friedrichs–Lewy (CFL) conditions for a rotating wake, we take advantage of the disk's axisymmetry and instead model the disk rotation by specifying velocity boundary conditions on the IB points that are consistent with rigid-body rotation. This is far more computationally efficient, as the highest relative velocity in the flow now scales with $U(1+\lambda)$ on the advancing side of the disk. This construction results in zero-velocity boundary conditions at large distances from the disk.

In continuous form, the governing equations and boundary conditions are given by

$$\frac{\partial \boldsymbol{u}}{\partial t} + (\boldsymbol{u}\cdot\nabla)\,\boldsymbol{u} = -\nabla p + \frac{1}{Re}\nabla^2\boldsymbol{u} + \int_{\Xi(t)} \boldsymbol{f}_{\Xi}(\xi,t)\delta(\boldsymbol{X}(\xi,t)-\boldsymbol{x})\,\mathrm{d}\xi, \tag{2.1}$$

$$\nabla\cdot\boldsymbol{u} = 0, \tag{2.2}$$

$$\int_{\mathbb{R}^3} \boldsymbol{u}(\boldsymbol{x},t)\delta(\boldsymbol{x}-\boldsymbol{X}(\xi,t))\,\mathrm{d}\boldsymbol{x} = \boldsymbol{u}_{\Xi}(\xi,t), \tag{2.3}$$

where $\boldsymbol{u}(\boldsymbol{x},t)$ is the fluid velocity and p is the pressure. The immersed surface is parametrised by ξ, and $\boldsymbol{u}_{\Xi}(\xi,t)$ is the velocity across its surface. Equation (2.3) represents the no-slip condition on the immersed surface, with $\boldsymbol{f}_{\Xi}(\xi,t)$ denoting the force density that is computed such that $\boldsymbol{u}(\boldsymbol{x},t)$ satisfies this condition, with $\delta(\boldsymbol{X}(\xi,t)-\boldsymbol{x})$ as the delta function that regularises the force onto the flow grid. These equations are solved on an unbounded domain, resulting in a decaying far-field boundary condition given by $\boldsymbol{u}(\boldsymbol{x},t)\to 0$ as $|\boldsymbol{x}|\to\infty$.

2.2. *Numerical set-up*

Figure 1 shows the top, side and upstream views of the simulation set-up. The computational grid is fixed relative to the IB points. Disk spin is about the disk axis of axisymmetry, defined as the y-axis for $\alpha = 0°$, with positive rotation ($\lambda > 0$) in the clockwise direction when viewed from above. Angle of attack is introduced by rotating the flow vector relative to the grid. The free stream flow is in the positive x direction. For spinning cases, where $\lambda > 0$, one side of the disk is advancing into the flow while the other side of the disk is receding away from the flow, named the advancing side and receding side, respectively (figure 1*c*). Note that although figure 1(*b*) denotes some finite thickness, we model the disk as infinitely thin using a single layer of IB points. In spite of this, by the nature of the regularisation of the IB forces onto the flow grid, there will be an apparent thickness, which will be discussed in more detail in § 2.3.5.

2.3. *Convergence studies*

While the IBLGF method has been verified and subjected to convergence tests extensively by Liska & Colonius (2017), it is necessary to select an appropriate resolution for the current studies. In this section, we describe the four resolution parameters: grid resolution, Δx; temporal discretisation, Δt; IB point spacing, Δs; and domain adaption threshold, ϵ. For each, we conduct a series of tests to confirm the convergence and then select a value to use in the production simulations. We evaluate the convergence of the disk aerodynamic forces for these resolution parameters for simulations at

Case	λ	$\Delta x/D$	$\Delta tU/D$	ϵ	$\overline{C_L}$	$\overline{C_D}$	ΔC_L	ΔC_D
A1	0	0.012	0.004	5×10^{-4}	0.565	0.376	0.013	0.003
A2	0	0.009	0.003	3.6×10^{-4}	0.578	0.374	0.010	0.002
A3	0	0.012	0.004	5×10^{-5}	0.561	0.374	0.015	0.003
A4	0	0.012	0.003	5×10^{-4}	0.565	0.376	0.013	0.003
A5	0	0.012	0.005	5×10^{-4}	0.567	0.378	0.013	0.003
B1	3	0.012	0.001	5×10^{-4}	0.863	0.525	0.079	0.020
B2	3	0.009	0.00075	3.6×10^{-4}	0.874	0.523	0.026	0.008
B3	3	0.012	0.001	5×10^{-5}	0.866	0.526	0.079	0.020

Table 1. Time-averaged lift and drag coefficients, $\overline{C_L}$ and $\overline{C_D}$, and peak-to-peak oscillation in lift and drag coefficients, ΔC_L and ΔC_D, with different spatial resolutions, $\Delta x/D$, time step, Δt , and adaptive threshold, ϵ. All simulations are performed at $Re = 500$ and $\alpha = 25°$. Cases A1–A5 are at $\lambda = 0$ and cases B1–B3 are at $\lambda = 3$. Cases A1 and B1 correspond to the base resolution used for the remaining data presented (but with time steps adjusted for the tip-speed ratio). Cases A2 and B2 are at a finer mesh resolution. Cases A3 and B3 are at a lower (more accurate) adaptive threshold. Cases A4 and A5 correspond to smaller and larger time step sizes, respectively.

$Re = 500$ and $\alpha = 25°$. The lift, drag and side force coefficients are defined as $(C_L, C_D, C_S) = (F_L, F_D, F_S)/((1/2)\rho U^2 \pi R^2)$, respectively, where F_L, F_D and F_S are the corresponding dimensional forces in the y, x and z directions, respectively. The rolling, pitching and yawing moment coefficient are defined as $(C_{MR}, C_{MP}, C_{MY}) = (M_R, M_P, M_Y)/((1/2)\rho U^2 \pi R^2 D)$, respectively, where M_R, M_P and M_Y are the corresponding dimensional moments. Note that computational length and velocity scales in the code are non-dimensionalised by the disk diameter, D, and the free stream velocity, U, respectively.

2.3.1. *Grid spacing, Δx*

Grid resolution comparisons by Liska & Colonius (2017) for flow over the flat plate at $Re = 300$ and $\alpha = 30°$ showed a 4 % difference in mean force coefficients for $\Delta x/D = 0.025$ when compared with finer resolution simulations having $\Delta x/D = 0.015$. To resolve the flow to a similar accuracy for different Reynolds numbers, we maintain the value of $(\Delta x/D)Re^{1/2}$ within the same range, based on the expected $O(Re^{-1/2})$ scaling of the laminar boundary layer thickness (Liska & Colonius 2017). Therefore, we select a nominal grid resolution of $\Delta x/D = 0.012$ for simulations at $Re = 500$, which gives approximately the same $(\Delta x/D)Re^{1/2}$ value as for the fine case in the verification studies by Liska & Colonius (2017). This gives approximately 83 grid points across the disk diameter.

To confirm the convergence at this grid resolution, we compare force coefficients between the base resolution, $\Delta x/D = 0.012$, and a finer resolution, $\Delta x/D = 0.009$. The resulting time-averaged lift and drag coefficients, $\overline{C_L}$ and $\overline{C_D}$, and the corresponding peak-to-peak oscillations in lift and drag coefficients, ΔC_L and ΔC_D, are shown in table 1 for both $\lambda = 0$ (cases A1–A2) and $\lambda = 3$ (cases B1–B2). Cases A1 and B1 use the base resolution ($\Delta x/D = 0.012$), while cases A2 and B2 use the fine grid resolution ($\Delta x/D = 0.009$). Note that for smaller grid spacing, the fractional adaptive threshold, ϵ, is scaled such that the absolute adaptive threshold, ϵ_{abs}, is held constant, because the maximum vorticity in the flow increases as the finer grid resolves flow closer to the disk surface, where vorticity is greatest. This means that between cases A1/B1 and A2/B2, ϵ_{abs} is roughly constant.

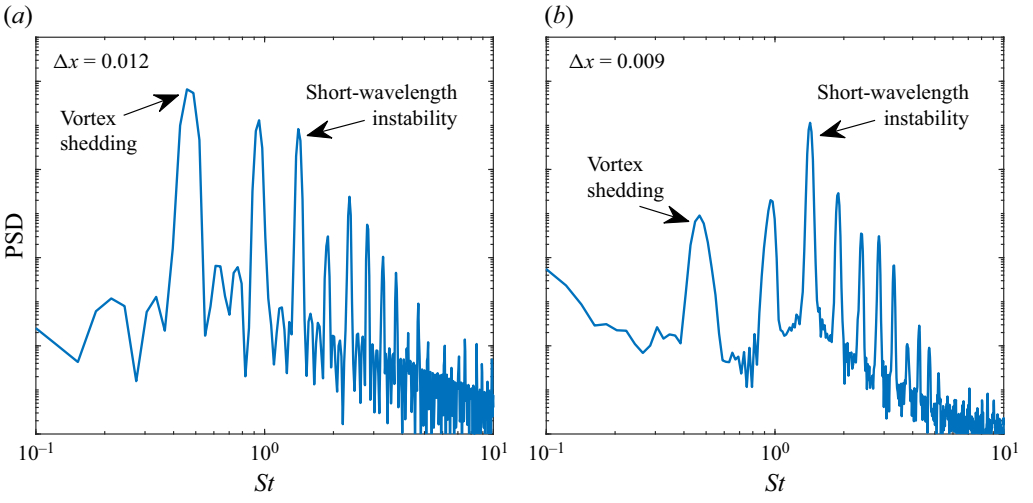

Figure 2. PSD for $Re = 500$, $\alpha = 25°$ and $\lambda = 3$ with grid resolutions of (*a*) $\Delta x/D = 0.012$ (case B1) and (*b*) $\Delta x/D = 0.009$ (case B2). The Nyquist frequencies are $St = 500$ and $St = 667$, respectively. Note that y-axes are logarithmic. Frequency bin size differs between the two plots.

For the non-spinning case, results are well converged for $\Delta x/D = 0.012$ (case A1). Mean lift values are within 3 % of those for the fine case $\Delta x/D = 0.009$ (case A2). The increased resolution leads to approximately a 20 % decrease in the peak-to-peak oscillation of the lift coefficient, ΔC_L, denoting a weakening of vortex shedding. This discrepancy is in the third decimal place. For the case of $\lambda = 3$, we see that the difference in mean lift is less than 2 % between the two resolutions (cases B1 and B2). The discrepancy is mostly in the peak-to-peak oscillations, ΔC_L and ΔC_D, which vary in the second decimal place (table 1). These error levels are in line with those from Liska & Colonius (2017), except for larger variations in the coefficient fluctuations at $\lambda = 3$. We note that the flat-plate convergence studies also show a decrease in fluctuation amplitude for increasing grid resolution (Liska & Colonius 2017).

To understand the discrepancy in the signal fluctuations, we analyse the power spectral density (PSD) of the lift signals. Figure 2 shows the PSD for these two different grid resolutions, allowing us to differentiate between the frequency peaks that contribute to the lift fluctuations. While the base grid-resolution case is dominated by a peak at $St \approx 0.5$, associated with vortex shedding, the energy for the same peak is approximately three orders of magnitude lower in the finer case. Both have peaks at a frequency $St \approx 1.4$, which we will later see corresponds to a short-wavelength, elliptic instability. The energy, integrated from the PSD, of the $St = 1.4$ peaks are within 5 % for both resolutions. Throughout this paper, peak energies are obtained by trapezoidal integration over five frequency bins centred on each peak (± 2 bins). This corresponds to a maximum integration width of $\Delta St = 0.13$ across all cases, although typically $\Delta St < 0.10$ or ± 0.05 on either side of the peak frequency. This method achieves >90 % convergence and/or $<10^{-6}$ error of the energy while minimising leakage from adjacent peaks. This indicates that the discrepancy in lift fluctuation is accounted for by the difference in vortex-shedding magnitude, while the energy of the short-wavelength instability is preserved. We elaborate on this point in § 2.3.5, where we discuss the effect of disk thickness on the vortex-shedding bifurcation point.

2.3.2. *Time step, Δt*

For all simulations, the time step is scaled based on the maximum relative disk-edge velocity to free stream velocity using $\Delta t < (\Delta x/3)U(1+\lambda)$, which ensures that the CFL number never exceeds one during the simulation. In practice, consistent with Liska & Colonius (2017), the CFL number remains below 0.6 in the long-time simulation after reaching a maximum of approximately 0.9 for the early time steps. For time steps satisfying the CFL condition, lift and drag values are converged to at least the third decimal place (see cases A1, A4 and A5 in table 1). This is a result of the second-order accuracy of the viscous integrating factor (IF) half-explicit Runge–Kutta (HERK) time integration scheme used (Liska & Colonius 2017).

2.3.3. *Immersed boundary point spacing, Δs*

The infinitely thin disk geometry is represented by a single layer of immersed-boundary points. These are generated using Distmesh, an unstructured-mesh generator developed by Persson & Strang (2004). The IB spacing is not uniform across all points but follows a bell-shaped distribution with up to $\pm 20\,\%$ from the mean spacing.

The distribution of IB point spacing in the disk mesh has implications for computational accuracy. Simulations by Kallemov *et al.* (2016) and Goza & Colonius (2017) showed that $\Delta s/\Delta x < 2$ is sufficient to ensure body impermeability. In addition, Liska & Colonius (2017) showed that $\Delta s/\Delta x > 1$ leads to an acceptable condition number for the Schur complement operator used to solve the IB formulation. When $\Delta s/\Delta x \lessapprox 1$, the discrete Schur complement operator can become non-singular leading to numerical instability (Liska & Colonius 2017). Therefore, we ensure that all IB point spacing throughout the mesh are restricted to the range $1 < \Delta s/\Delta x < 2$. Specifically, we use $\overline{\Delta s}/\Delta x \approx 1.6$ to minimise the number of IB points, and thus the computational cost, without sacrificing accuracy.

2.3.4. *Adaptive domain threshold parameter, ϵ*

The computational domain adapts to regions of the grid that contain non-negligible amounts of vorticity and/or the source term in the Poisson equation (Liska & Colonius 2016). Specifically, the adaptive threshold, ϵ, is a fractional parameter based on the maximum vorticity magnitude seen in the entire computational domain and determines the amount of domain truncation. In practice, $0 < \epsilon < 1$, where $\epsilon = 0$ means the computational grid would extend infinitely (adaption to all values of vorticity). For simulations in the present study, we use $\epsilon = 5 \times 10^{-4}$, matching studies by Liska & Colonius (2017).

In table 1, we compare time-averaged lift and drag coefficients for the base adaptive threshold at $\epsilon = 5 \times 10^{-4}$ and a finer adaptive threshold at $\epsilon = 5 \times 10^{-5}$. Comparing aerodynamic coefficients for $\lambda = 0$ (cases A1 and A3) and $\lambda = 3$ (cases B1 and B3) shows that the mean values and their fluctuations show excellent agreement for a tenfold difference in adaptive threshold, with differences only observed in the third decimal place. This agreement continues for $\Delta x/D = 0.009$ as well. Note that the noise levels in the aerodynamic signals scales approximately linearly with the adaptive threshold due to the discrete addition and removal of computational blocks as the domain adapts. For steady signals at $\Delta x/D = 0.012$, the noise level in lift is at most ± 0.001 for $\epsilon = 5 \times 10^{-4}$ and decreases to ± 0.0001 for $\epsilon = 5 \times 10^{-5}$.

2.3.5. *Effect of thickness on the vortex shedding bifurcation*

While the effect of thickness is not formally explored in this paper, we take a moment to discuss its potential effects on the simulation results, as it may account for the discrepancy

in lift fluctuations with changing grid resolution presented in § 2.3.1. Disk thickness has been shown to change the value of critical points of disk flow bifurcation and even the nature of the bifurcation (Meliga, Chomaz & Sipp 2009; Auguste, Fabre & Magnaudet 2010; Chrust *et al.* 2015; Gao *et al.* 2018).

While we model the disk using a single layer of IB points, the regularisation of the IB forces onto the flow grid using a delta function results in a narrow strip of grid points surrounding the IB points over which the disk surface forcing influences the flow directly. While not directly equivalent to a physical disk thickness, this results in an apparent thickness for the disk. Specifically, we use a smoothed 3-point delta function which has a support of up to two grid points in either direction (Roma, Peskin & Berger 1999; Yang *et al.* 2009). As a result, the apparent disk thickness scales with the grid spacing, resulting in a thinner disk for finer resolutions. For $\Delta x/D = 0.012$, this gives an approximate upper limit of the apparent thickness of $t_d = 0.048$ (or aspect ratio $\chi \approx 21$). For the finer resolution $\Delta x/D = 0.009$, the apparent thickness is at most $t_d = 0.036$ ($\chi \approx 28$). This makes it challenging to fully separate the effects of thickness and grid resolution since they vary together by the nature of the IB method. However, the changing force coefficient fluctuations with changing grid resolution observed in § 2.3.1 are consistent with the trends seen in the literature for the effect of thickness. Comparisons between results from Chrust *et al.* (2015) and Gao *et al.* (2018) indicate that for $\alpha < 40°$, a higher disk aspect ratio (thinner disk) increases the critical Reynolds number at which the vortex-shedding bifurcation occurs, i.e. it stabilises the flow. Consistent with this effect, we observe decreased lift and drag fluctuation amplitudes as the grid spacing decreases for both $\lambda = 0$ and $\lambda = 3$ (table 1). As a side note, Liska & Colonius (2017) also observe modest decreases in the lift and drag fluctuations with decreasing grid spacing, possibly due to thickness effects on vortex shedding as well.

At $Re = 500$ and $\lambda = 0$, the critical angle of attack is roughly 24.3° (estimated in § 2.4.2). Therefore, because the present simulations at $\alpha = 25°$ are very close to the critical point, we can expect vortex shedding – and the resulting lift- and drag-fluctuation amplitudes – to be particularly sensitive to thickness effects or potential underresolution. In § 2.3.1, for $\lambda = 3$, the PSD analysis between the base and fine resolution cases showed that vortex shedding was significantly weakened in the fine case, with little effect on the strength of the short-wavelength instability. We expect the elliptic instability, which is an instability in the tip vortices, to be relatively independent of changing thickness as it depends primarily on the tip-vortex parameters rather than on the exact geometry of the disk. However, we do recognise that the decrease in vortex-shedding strength is much larger at $\lambda = 3$ than at $\lambda = 0$, so we do not rule out that there may be some underresolution at play as well for high TSRs. Potential underresolution would depend on the effect of spin on the boundary layer thickness to be resolved. While the boundary layer caused by a rotating disk (in quiescent flow) is significantly larger than that for a traditional flat plate laminar boundary layer, the rotating disk boundary layer continues to decrease with increasing TSR and may decrease the grid spacing required to accurately resolve the flow close to the disk.

In summary, thickness effects seem to account for decreasing vortex-shedding strength, which is consistent with results in the literature, though there may also be some degree of underresolution at high TSRs. In production runs for this work, we use a resolution of $\Delta x/D = 0.012$, which represents an apparent thickness of $t_d \approx 0.048$ or aspect ratio of $\chi \approx 21$. This is slightly underresolved for the purposes of representing an infinitely thin disk, but allows us to explore high TSRs that would otherwise be far more computationally intensive. This allows us to explore new flow regimes that appear and understand the mechanisms behind them. The limitation in accurately defining and maintaining a thickness for the disk means that there remains uncertainty in the precise critical points

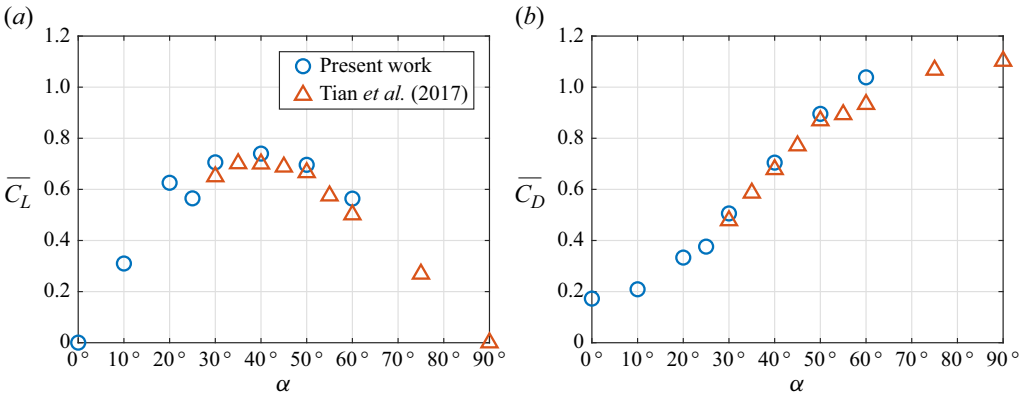

Figure 3. Time-averaged lift and drag coefficients, $\overline{C_L}$ and $\overline{C_D}$, for the non-spinning disk at $Re = 500$. The signal length for computing time-averages is at least 170 tU/D for unsteady cases, leading to standard error values at most 2×10^{-4}. The standard error is largest for the quasi-periodic and chaotic cases at higher angles of attack.

of bifurcation and aerodynamic forces, specifically with respect to the actual thickness. However, we maintain that the key trends and flow features are preserved with the chosen resolution.

2.4. *Comparisons with previous simulations for the non-spinning disk*

In this section, we verify our results by comparing aerodynamic forces and critical points with past DNS results for non-spinning disks by Chrust *et al.* (2015), Tian *et al.* (2017) and Gao *et al.* (2018). These studies focus on high angles of attack $\alpha \geq 30°$. To overlap with some of these results, we make comparisons over the range $30° \leq \alpha \leq 60°$. Unfortunately, we are not aware of any spinning disk cases to compare to for a flat disk at these Reynolds numbers.

2.4.1. *Aerodynamic force comparisons*

In figure 3, we compare mean lift and drag values for $Re = 500$ and $\lambda = 0$ over a range of angles of attack with those reported by Tian *et al.* (2017). Good agreement is observed with discrepancies ranging from 3 % to 12 % for both lift and drag values. We observe a small dip in C_L of approximately 0.06 units from $\alpha = 20°$ to $\alpha = 25°$. This is greater than the error estimate (± 0.01 units) so we expect it to be a physical observation. This coincides with the transition from steady flow to vortex shedding. This dip may be associated with this transition in the wake stability or also a symptom of the flow's sensitivity close to the critical point, as we will find that $\alpha_c = 24.3°$ (§ 2.4.2). Direct comparisons to circular disk flows are not available. However, Taira *et al.* (2007) observed a similar dip at the same angle of attack for two-dimensional flow over a flat plate at $Re = 100$. However, Taira & Colonius (2009) did not observe a dip in lift coefficient for three-dimensional flow over a rectangular flat plate for aspect ratios from one to four.

2.4.2. *Critical Reynolds number comparisons*

Chrust *et al.* (2015) and Gao *et al.* (2018) determined the critical Reynolds number for the first (Hopf) bifurcation for a range of angles of attack. To compare with their results, we estimate the critical Reynolds number by making use of the fact that near a supercritical Hopf bifurcation, the peak-to-peak amplitudes of the oscillation in

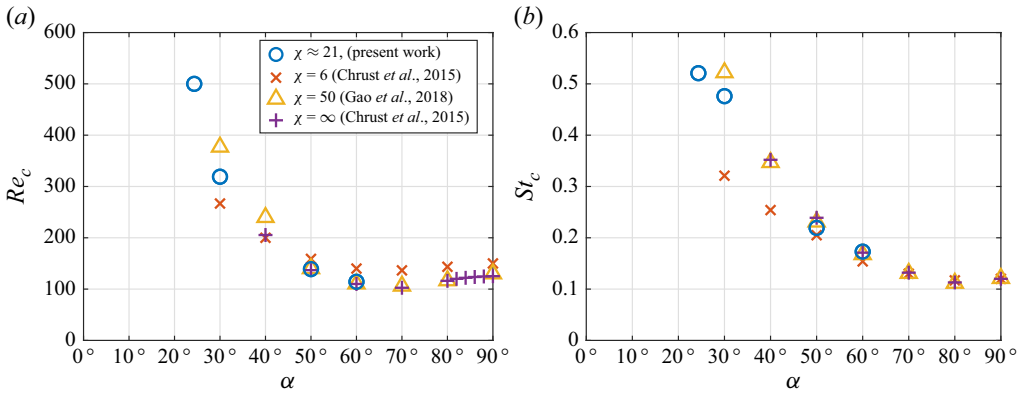

Figure 4. (*a*) Critical Reynolds number and (*b*) critical Strouhal number against angle of attack for the supercritical Hopf bifurcation from steady to periodic vortex shedding.

aerodynamic coefficients are directly proportional to the square root of the degree of criticality of the bifurcation parameter (Ghaddar *et al.* 1986; Pereira & Sousa 1993).

In figure 4, we compare the values we obtain for critical Reynolds number, Re_c, and critical Strouhal number, St_c, as a function of angle of attack to values reported in the literature for various disk aspect ratios in the range $6 \leq \chi \leq \infty$ by Chrust *et al.* (2015) and Gao *et al.* (2018). The values show great agreement, particularly at high angles of attack. For low angles of attack, the critical Reynolds number varies with the disk aspect ratio. For $\alpha = 30°$, $Re_c = 320$ for the present work for an estimated aspect ratio $\chi \approx 21$. This falls between the values from Gao *et al.* (2018) for the thin disk ($Re_c = 377$ for $\chi = 50$) and from Chrust *et al.* (2015) for the thick disk ($Re_c = 267$ for $\chi = 6$). By comparing these cases, we see that a thicker disk results in a lower critical Reynolds number for $\alpha < 40°$, but higher critical Reynolds number for $\alpha > 40°$. These results are consistent with the decreasing ΔC_L and ΔC_D observed as we used a finer mesh (and thus effectively thinner disk) in § 2.3.1.

3. Spinning disk aerodynamics and wake structure

Past studies have identified several wake regimes for flow over non-spinning inclined disks at $Re = O(10^2)$ (Chrust *et al.* 2015; Tian *et al.* 2017; Gao *et al.* 2018). Both Reynolds number and angle of attack serve as bifurcation parameters that take the flow from steady to chaotic as they are increased. The goal of this section is to explore the effect of spin on these bifurcations. We study the changing aerodynamics and wake instabilities in this same Re–α parameter space. To this end, we simulate the flow through a range of TSRs from zero to three, while fixing the Reynolds number and angle of attack at $Re = 500$ and $\alpha = 25°$. With no spin ($\lambda = 0$), this flow configuration is supercritical with respect to the first bifurcation ($\alpha_c = 24.3°$ at $Re = 500$) and exhibits mild vortex shedding. By analysing the changing frequency content and visualising vorticity isosurfaces, we can identify several distinct wake regimes of interest.

3.1. *Aerodynamic forces for a spinning disk*

Figure 5 shows the long-time time-varying and time-averaged lift and drag coefficients as λ varies. Both lift and drag follow similar trends with increasing λ, though the mean value and fluctuation amplitudes remain higher for lift than for drag throughout. The mean lift and drag both increase monotonically as λ is increased. The fluctuations in lift and drag

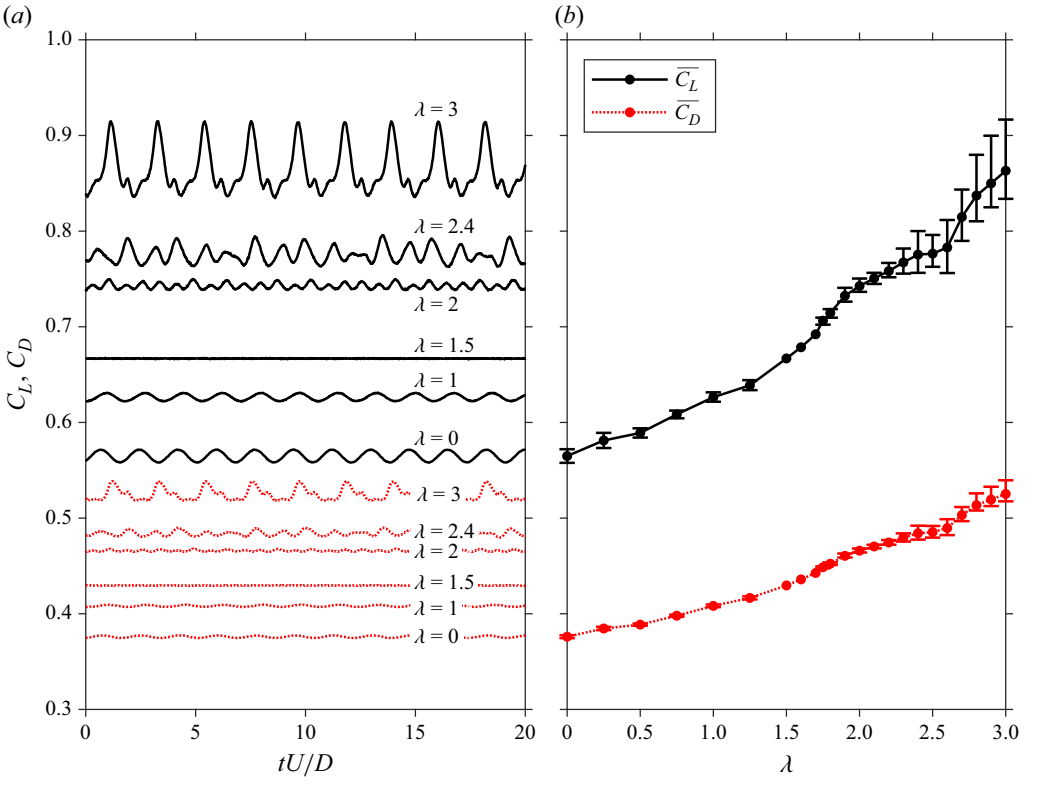

Figure 5. (*a*) Instantaneous lift and drag coefficients, C_L and C_D, and (*b*) time-averaged lift and drag coefficients, $\overline{C_L}$ and $\overline{C_D}$, for the spinning disk at different tip-speed ratios, λ, for $Re = 500$ and $\alpha = 25°$. Lift coefficient values are denoted by solid black lines and drag coefficient values are denoted by dotted red lines. Error bars indicate the min-to-max range of coefficient values for unsteady cases. The signal length for computing time averages is at least 70 tU/D for unsteady cases, leading to standard error values at most 7×10^{-5}.

over time show a more complex and non-monotonic behaviour. For the non-spinning case at $\lambda = 0$, at which the flow is only slightly supercritical with respect to the wake (vortex-shedding) instability, the lift fluctuations are small in amplitude and monochromatic. As λ increases to 1.5, the oscillation amplitude decreases to zero, while the fluctuations remain monochromatic. For cases from $\lambda = 1.5$ to $\lambda = 1.7$ inclusive, the lift and drag values are steady, indicating a steady flow, as vortex shedding is suppressed.

For $\lambda \gtrapprox 1.75$, the flow becomes unsteady again. From $\lambda = 1.7$ to $\lambda = 3$, the fluctuation amplitudes generally increases. Just past $\lambda = 1.7$, the fluctuations are again monochromatic with a similar frequency as $\lambda < 1.5$, indicative of flow being once again slightly supercritical. As λ is further increased, the flow remains in a limit cycle behaviour. However, the waveforms become more complex and non-monochromatic, indicating that the flow passes through additional bifurcations. We will later identify a short-wavelength elliptic instability at these high TSRs.

3.2. *Wake regimes for a spinning disk*

The transition to unsteadiness in force and moment coefficients is suggestive of instabilities. To better understand the flow phenomenon that give rise to these trends, we examine the frequency content of the aerodynamic forces alongside visualisations of the wake structure. Figure 6 visualises isosurfaces of streamwise and spanwise vorticity for selected values of λ between zero and three.

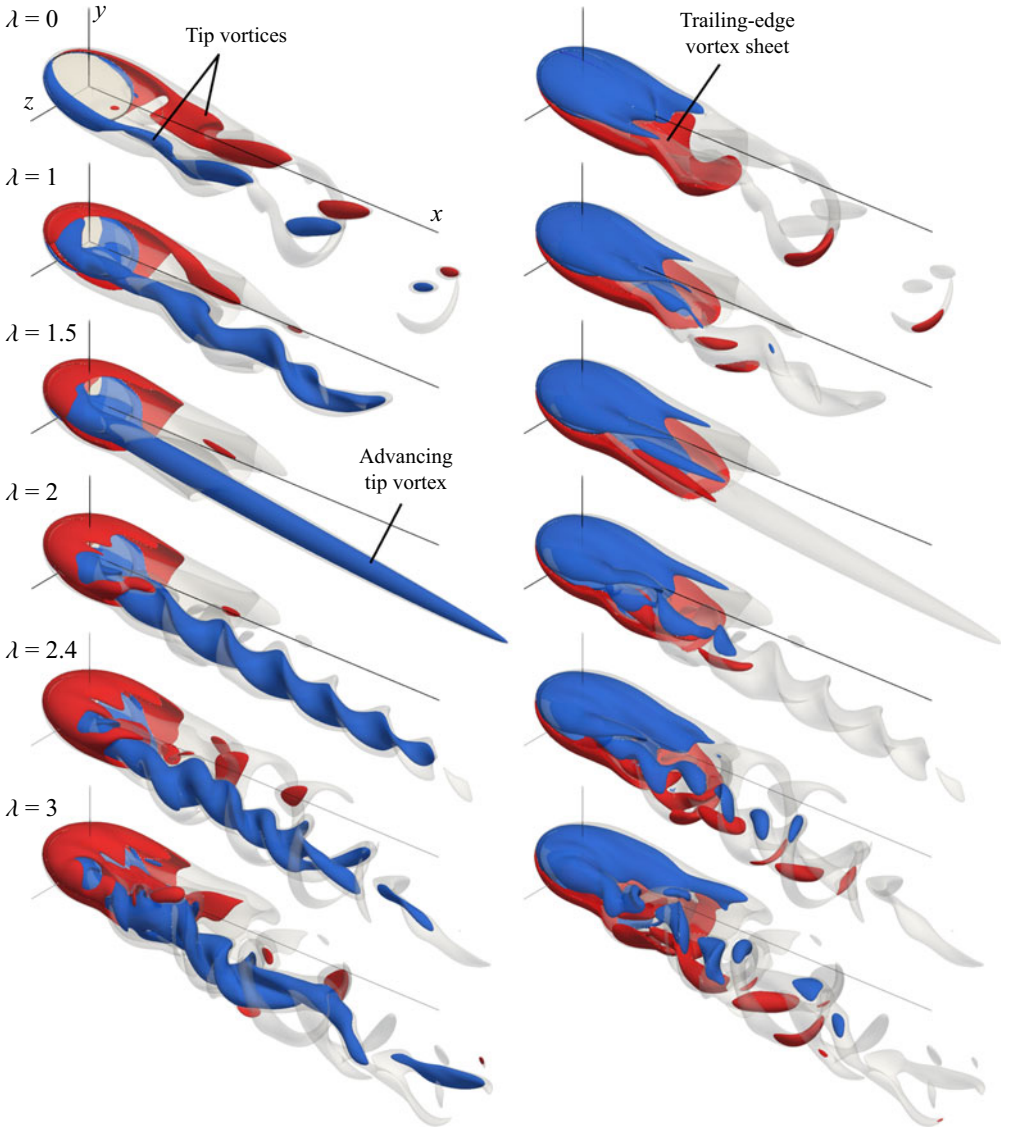

Figure 6. Isosurfaces of vorticity for the disk at $Re = 500$ and $\alpha = 25°$ for $\lambda = 0$, 1, 1.5, 2, 2.4 and 3. The free stream velocity is in the positive x-direction (approximately top left to bottom right) with the disk rotating clockwise from above. Semi-transparent grey isosurfaces are vorticity magnitude, $||\boldsymbol{\omega}|| = 3$. Streamwise vorticity, ω_x (left column) and spanwise vorticity, ω_z (right column) are shown in opaque red and blue for positive (+3) and negative (−3) values, respectively. The x-, y- and z-axes reference lines are $5D$, $1D$ and $1D$ long, respectively.

These visualisations reveal several distinct wake regimes, classified based on the flow phenomena exhibiting the dominant frequency amplitude in the power spectra of the coefficient of lift signal (figures 7 and 8).

(i) Regime 1 ($0 \lessapprox \lambda \lessapprox 1.9$): dominated by a standard wake instability with periodic hairpin-vortex shedding ($St \approx 0.5 - 0.6$), modulated from slightly supercritical to subcritical and back to supercritical.

(ii) Regime 2 ($1.9 \lessapprox \lambda \lessapprox 2.2$): characterised by the emergence and dominance of a short-wavelength instability ($St \approx 1.2 - 1.4$) that closely resembles an elliptic instability mode.
(iii) Regime 3 ($2.2 \lessapprox \lambda \lessapprox 3$): a regime in which the wake exhibits mixed features of both the wake instability and the short-wavelength instability.

Figure 7 shows Welch's PSD estimate of the lift coefficient, which helps to distinguish between different instabilities in the wake. By observing changes in the wake structure in a series of visualisation snapshots of the wake, we can associate the Strouhal numbers, St, from the PSD peaks with different wake behaviours. To reveal trends in the changing frequency content with increasing TSR, we determine the frequency peaks with total energies exceeding a certain threshold and plot them against λ (figure 8). The marker sizes are scaled based on the peak's total energy, which is found by integrating over each peak in Welch's PSD estimate. The maximum frequency bin size is $\Delta St = 0.04$. Peaks are relatively distinct and compact, with their energies converging to at least 90 % of the total energy for integration bin sizes of approximately $\Delta St = 0.1$.

For the non-spinning disk ($\lambda = 0$), the wake instability causes the trailing-edge vortex sheet to roll up and shed from the disk periodically. The roll up interacts with segments of the tip vortices to form spanwise-symmetric hairpin vortices which loop across the centre plane with legs extending towards the disk (grey isosurfaces in figure 6). The power spectrum indicates monochromatic frequency content associated with the wake instability. For $\lambda = 1$, the magnitude of the single frequency peak associated with vortex shedding has decreased from the non-spinning case (figure 7). The wake loses its spanwise symmetry, with the hairpin vortices becoming relatively more distinct on the advancing side of the disk ($z > 0$ side) compared with the receding side ($z < 0$ side). The frequency of these fluctuations is $St \approx 0.55$ and remains relatively unchanged between $\lambda = 0$ and $\lambda = 1.5$ (figure 8).

At $\lambda = 1.5$, vortex shedding is suppressed and the flow is again steady, indicating that the flow is subcritical with respect to the wake instability (figure 6). This behaviour and the corresponding lack of hysteresis is consistent with the standard view of the wake instability arising as a supercritical Hopf bifurcation. The trailing-edge vortex sheet no longer rolls up. This vortex-shedding suppression persists in a range from roughly $\lambda = 1.5$ to $\lambda = 1.7$ (figure 8). The tip vortex on the advancing side of the disk ($z > 0$) is significantly strengthened, while that on the receding side is more diffuse. This vorticity distribution and the mechanism behind the stabilising effect is discussed in detail in § 4.

While vortex-shedding is stabilised for low to moderate TSRs, higher TSRs excite a short-wavelength instability (figure 6). For $1.9 \lessapprox \lambda \lessapprox 2.2$, high-frequency content at $St \approx 1.3$ dominates the spectra (figure 8). This corresponds to a corkscrew-shaped instability in the advancing tip-vortex core, with regular 'braids' of vorticity twisting around themselves (figure 6). The wavelength of this instability is of the same order as the inter-tip-vortex distance, making its wavelength short relative to the wavelength of vortex shedding, which is approximately 2–3 times greater. As λ increases through this narrow range of $1.9 < \lambda < 2.2$, the wavelength decreases slightly and the frequency increases slightly as well. The frequencies match closely with twice the rotation frequency of the disk rotation (figure 8). For $\lambda = 2$, most of the energy of the flow is associated with this instability at $St = 1.31$. This short-wavelength instability has a frequency approximately 2.5 times that of the vortex-shedding frequency. Based on the strong qualitative resemblance, we identify this short-wavelength instability as the elliptic instability, specifically the $(-2, 0, 1)$ principal mode (Lacaze, Ryan & Le Dizès 2007). Appendix A provides further evidence for this identification, including the comparison of modes using spectral proper orthogonal

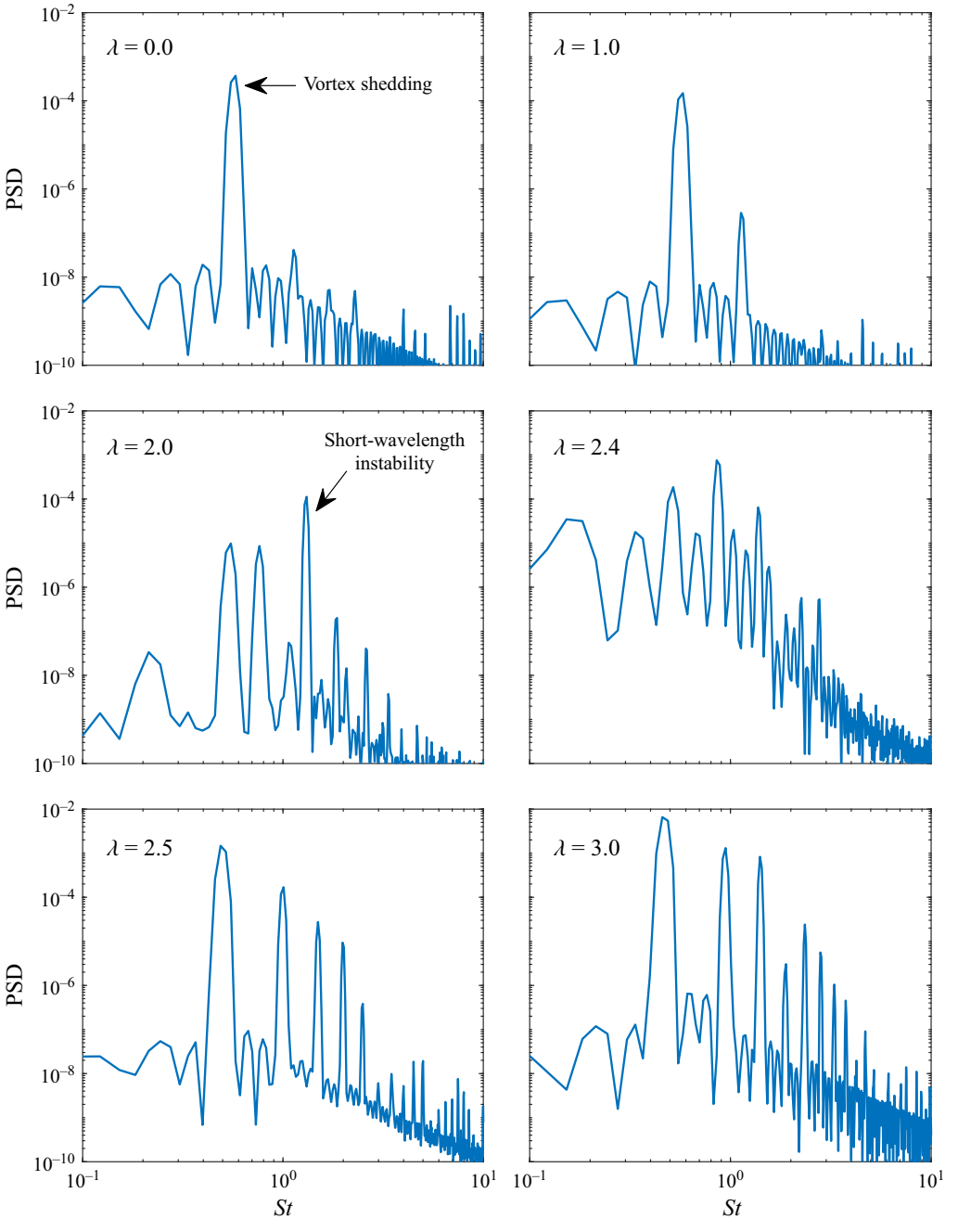

Figure 7. Welch's PSD estimate of the lift trace for the disk at $Re = 500$ and $\alpha = 25°$ for various λ. Since all cases are performed for the same time period, the frequency bin sizes are identical, with a frequency resolution of $\Delta St = 0.03$. Thus, the y-axes are arbitrary, but equivalent logarithmic scales. The Nyquist frequency is inversely proportional to the time step size, ranging from $St = 125$ for $\lambda = 0$ to $St = 500$ for $\lambda = 3$. We omit the PSD for the steady $\lambda = 1.5$ case, which lies below the lower limit of the y-axes and consists of frequency content from noise in the signal.

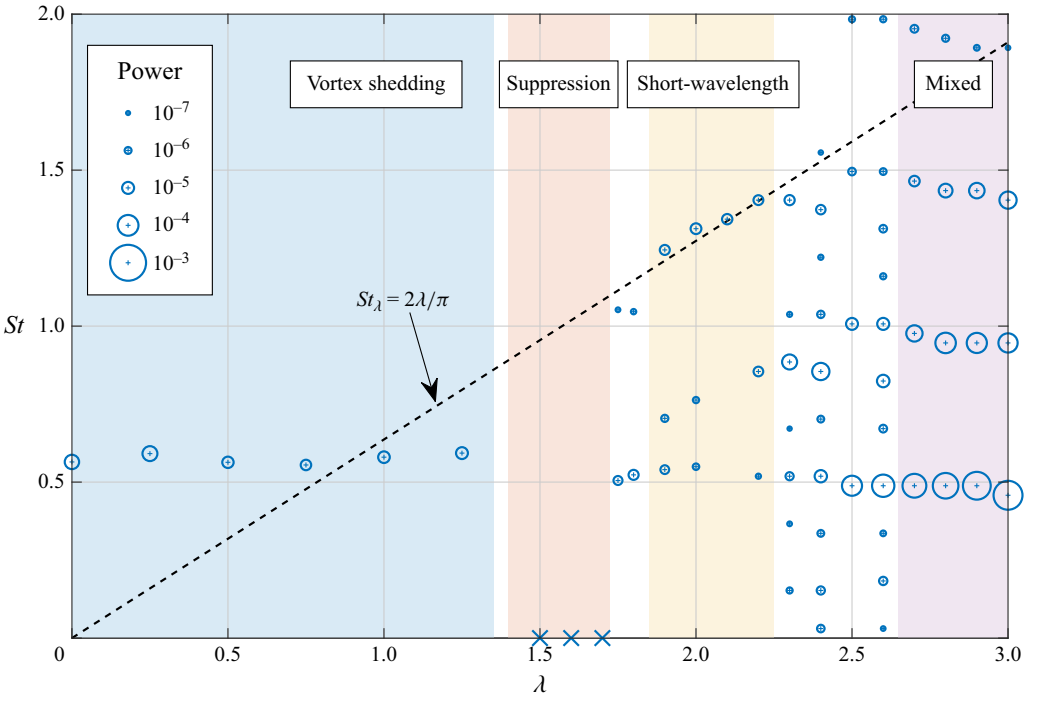

Figure 8. Frequency peaks from Welch's method against λ for the lift coefficient trace at $Re = 500$ and $\alpha = 25°$. Marker size is logarithmically scaled based on the integrated power from the PSD peak. Only peaks with power greater than 10^{-7} are plotted. The dashed line indicates twice the Strouhal number associated with the spin ($St_\lambda = 2\lambda/\pi$). Cross markers indicate steady cases. Regions are shaded by regime, namely vortex shedding (blue), suppression (red), short-wavelength instability (yellow), and mixed vortex shedding and short-wavelength instability (purple).

decomposition (SPOD) and comparison of flow parameters within the advancing tip vortex with values required for resonance of the elliptic instability.

While the short-wavelength instability persists for $1.9 \leq \lambda \leq 3$, for $\lambda > 2.3$, the vortical structures in the wake become more complicated, although they still exhibit strongly periodic behaviour (figure 8). For $\lambda \geq 2.3$, additional lower frequency flow structures appear alongside the short-wavelength instability. The dominant frequency for $\lambda = 2.3$ and $\lambda = 2.4$ is $St \approx 0.9$. Meanwhile, for $2.5 \leq \lambda \leq 3$, the dominant frequency is $St \approx 0.5$, which is close to the vortex shedding frequency at low TSR (figure 8). This appearance of the power spectra peak around $St = 0.5$ corresponds to the non-planar-symmetric vortex shedding of the trailing-edge vortex sheet that extends from the advancing tip vortex and loop partially towards the receding side. This results in a transitionary region for $2.3 \leq \lambda \leq 2.6$, where the spectra are quite colourful, with many distinct peaks appearing. Although we observe distinct PSD peaks at similar frequencies to vortex shedding and short-wavelength instability when observed in isolation, when they occur together, they interact nonlinearly, which can impact the precise frequency of the peaks.

For $2.5 \lessapprox \lambda \lessapprox 3$, we see strong harmonic behaviour, with many or all of the frequency peaks occurring at harmonics of the dominant frequency at $St \approx 0.5$ (figure 7). This suggests some coupling between the vortex shedding and short-wavelength instability. Upon closer inspection, we can see that the legs of the shedding hairpin vortices align with braids of the elliptic instability (figure 6). For $2.7 \leq \lambda \leq 3$, the frequencies are more organised and form harmonics of one another, indicating even stronger coupling. There are

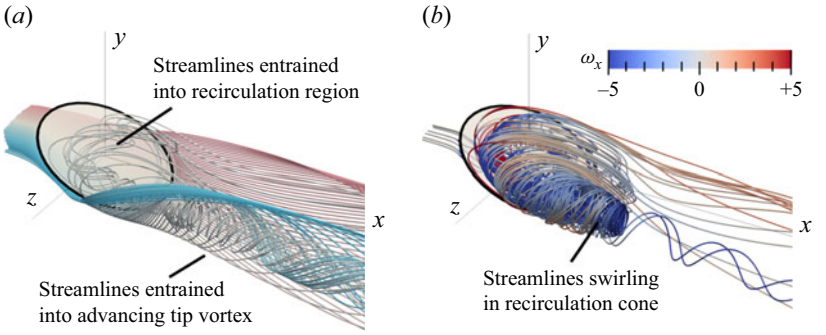

Figure 9. Visualisations of streamlines (or pathlines) for steady flow over the disk at $Re = 500$, $\alpha = 25°$ and $\lambda = 1.5$. The free stream velocity is in the positive x-direction (approximately top left to bottom right). In panel (a), streamlines are seeded along a spanwise line below the disk with a normal distance of $0.05D$, coloured by particle number, and in panel (b), streamlines are seeded in a ring parallel to the disk with a normal distance $0.1D$ and diameter $0.5D$, coloured by streamwise vorticity.

also irregular globules of vorticity being shed from the leading-edge vortex sheet, which has accumulated more streamwise vorticity as TSR has been increasing.

4. Vortex-shedding suppression by spin

To understand the mechanism for vortex shedding suppression, we visualise streamlines and vortex lines to elucidate how the distribution of vorticity in the wake changes as TSR increases. Note that for the cases presented in this section, the flows are steady, so streamlines are equivalent to pathlines. For streamlines passing close to the pressure side of the disk, most particles are entrained into the tip vortices (figure 9a). We see significant spanwise-outward velocity in the trailing-edge vortex sheet, induced by the entrainment of the tip vortices. Overall, the entrainment is skewed towards the advancing side due to the preferentially strengthened advancing tip vortex. There is also a narrow region of fluid that is entrained into the advancing tip vortex and then proceeds to swirl upstream into the recirculation region.

Streamlines that all pass through the recirculation region are shown in figure 9(b). Compared with the non-spinning case, the recirculation region elongates along the advancing side of the disk, while shortening on the receding disk side. This follows from the differential in local Reynolds number on either spanwise side of the disk. The recirculation region takes on a cone-like shape that shares many similarities with the flow profile caused by a rotating disk in quiescent flow (non-translating), which exhibits a spiralling, viscous pump action that draws in fluid towards the rotating disk. This cone of swirling fluid has its nose shifted into the advancing tip vortex. This is a result of the match in orientation of rotation in both the recirculation region and the advancing tip vortex (streamwise negative). The flow in the recirculation region swirls around and towards the disk.

The rigid-body rotation of the disk generates vorticity on both the pressure and suction surfaces. Examining the resulting vortex lines at $Re = 500$, $\alpha = 25°$ and $\lambda = 1.5$ (figure 10) demonstrates how vorticity convects in the wake for inclined flow. Vorticity from the top disk surface contributes to negative streamwise vorticity in the wake, primarily on the advancing side of the disk, following the alignment of the recirculation region towards the advancing side of the disk as well. The vortex lines extend from the suction surface of the disk into the wake and eventually loop back towards the disk. Following the orientation of the recirculation cone into the advancing-side tip vortex, the vortex lines originating

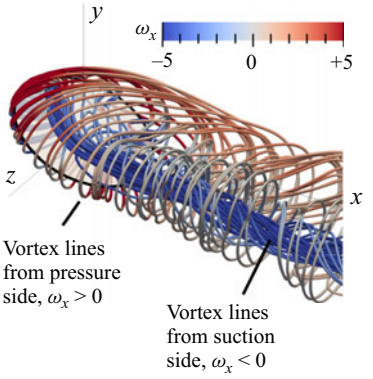

Figure 10. Visualisations of vortex lines for steady flow over the disk at $Re = 500$, $\alpha = 25°$ and $\lambda = 1.5$. The free stream velocity is in the positive x-direction (approximately top left to bottom right). Vortex lines extend from the suction side of the disk, seeded in a ring parallel to the disk with a normal distance $0.1D$ and diameter $0.5D$, and are coloured by streamwise vorticity, ω_x. The maximum length of vortex lines is $40D$. Vortex lines eventually loop back towards the disk.

from the top surface of the disk extend directly into the advancing tip vortex. However, vortex lines from the bottom surface are more diffused in the wake, distributed into both the receding tip vortex, and the leading-edge and trailing-edge vortex sheets. The spanwise-outward motion noted from the streamlines (figure 9*a*) helps to entrain vorticity from the trailing-edge vortex sheet around the advancing tip vortex and we see these vortex lines circle the vortex core.

While the magnitude of vorticity generated from the disk is the same for both surfaces, their orientation and how they advect into the wake differ greatly. Vortex lines from the top surface have the same streamwise sign as the advancing tip vortex, while vortex lines from the bottom disk surface have the same streamwise sign as the receding tip vortex. Since vortex lines from the top surface enter into the cone-shaped recirculation region, they are then fed into the advancing tip vortex directly, greatly strengthening the advancing tip vortex. However, vorticity from the bottom disk surface enter the wake from outside the recirculation region and so are more distributed around the tip vortices and trailing-edge vortex sheet. This leads to the behaviour observed in the vorticity-isosurface visualisations, where the advancing tip vortex dominates and the receding tip vortex is more diffuse. The increased circulation in the tip vortices increases downwash above the disk, so the leading edge vortex sheet hugs closer to the disk (figure 6). It also induces a significant spanwise-outward flow in the trailing-edge vortex sheet, helping to advect vorticity in the trailing-edge vortex sheet outwards. This diffusion of vorticity in the trailing-edge vortex sheet prevents its roll up, thus suppressing roll up.

4.1. *Unsteadiness at high tip-speed ratios*

Vortex shedding suppression persists until $\lambda \gtrapprox 1.75$, at which point unsteadiness in the wake resurfaces. The high-frequency content is associated with elliptic instability. Meanwhile, the low-frequency content corresponds to the reappearance of vortex shedding, which continues to grow with TSR. This means that rotation serves to modulate the flow from subcritical to supercritical with respect to the vortex shedding instability. A potential explanation for the reappearance of vortex shedding is related to the addition of vorticity into the wake by the disk rotation. Previously, we discussed that some of this vorticity enters the tip vortices, which in turn helps them to dissipate vorticity in

the trailing-edge vortex sheet before it rolls up. At the same time, some vorticity from the bottom side of the disk ends up in the trailing-edge vortex sheet (figure 10). As TSR increases, the strength of the trailing-edge vortex sheet increases as well. Whether or not the trailing-edge vortex sheet rolls up may then be a function of the competing effects of the spanwise convection of vorticity out of the trailing-edge vortex sheet and the addition of vorticity into the trailing-edge vortex sheet.

4.2. *Effect of spin on vortex shedding for other Reynolds number and angle of attack combinations*

The present work focuses on the effects of spin at $Re = 500$ and $\alpha = 25°$, chosen due to the proximity to the critical angle of attack of $\alpha_c \approx 24.3°$. However, we observe that vortex-shedding suppression and flow regime modification by spin is possible at a range of flow Reynolds numbers and angles of attack, including in cases further from the critical point where vortex-shedding strength is higher.

To demonstrate this, we consider representative cases in the non-spinning, (Re,α) parameter space which exhibit different flow regimes at different offsets from the critical Reynolds number:

(i) $Re = 500$ and $\alpha = 30°$ ($Re_c = 319$, periodic vortex shedding);
(ii) $Re = 120$ and $\alpha = 60°$ ($Re_c = 114$, periodic vortex shedding);
(iii) $Re = 300$ and $\alpha = 50°$ ($Re_c = 139$, periodic vortex shedding with low-frequency modulation).

Flow over the disk at $Re = 500$, $\alpha = 30°$ and $\lambda = 0$ exhibits periodic vortex shedding. Keeping the Reynolds number fixed at 500, the flow would transition to periodic vortex-shedding with low-frequency modulation at approximately $\alpha = 34°$ (Gao *et al.* 2018). Figure 11 shows the changing vorticity isosurfaces in the wake for $Re = 500$ and $\alpha = 30°$ as TSR increases from zero to two. The strength of vortex shedding at $\lambda = 0$ is visibly greater compared with that for $\alpha = 25°$, with larger, higher magnitude vortical structures that persist further downstream. At $\lambda = 1$, the spanwise planar symmetry breaks, with stronger trailing-edge vortex-sheet roll up on the advancing side of the disk. The frequency of vortex-shedding increases from $St = 0.59$ at $\lambda = 0$ to $St = 0.69$ at $\lambda = 1$. At $\lambda = 2$, the flow is steady, with an unbroken tip vortex on the advancing side that is much stronger than the receding-side tip vortex. While vortex-shedding suppression is present at $\alpha = 30°$, it occurs at a higher TSR compared with the $\alpha = 25°$ case.

Next, we examine the weakly vortex-shedding case at $Re = 120$ and $\alpha = 60°$ to explore the effect of spin at higher angles of attack. This flow configuration is close to the critical Reynolds number of $Re_c = 114$. Figure 12 shows vorticity isosurfaces for $Re = 120$ and $\alpha = 60°$ as TSR increases from zero to two. For the non-spinning case, the flow is supercritical ($Re_c = 114$) and exhibits periodic vortex shedding ($St = 0.17$). Because of the low Reynolds number and proximity to the critical point, the strength of the vortical structures is much weaker than in the $Re = 500$ cases considered. Note that the vorticity contour levels have been decreased correspondingly. The red isosurface of z-vorticity shows the trailing-edge vortex sheet beginning to oscillate before rolling up and shedding into the wake. Isosurfaces of x-vorticity show tip vortices on both the sides of the disk.

For $\lambda = 0.5$ and $\lambda = 1$, the flow is steady and the trailing-edge vortex sheet does not roll up. In contrast to the non-spinning case, the advancing tip vortex is greatly strengthened, while the receding tip vortex disappears from the wake. The advancing tip vortex extends past the spanwise centre plane. Steady flow is observed at both $\lambda = 0.5$ and $\lambda = 1$,

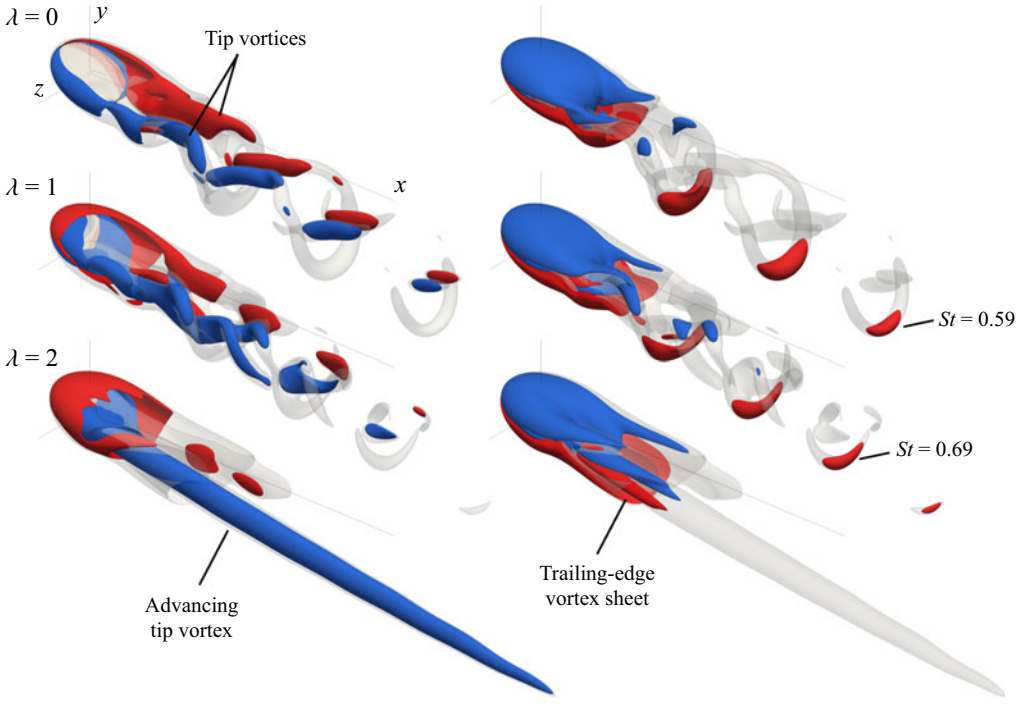

Figure 11. Isosurfaces of vorticity for the disk at $Re = 500$ and $\alpha = 30°$ for $\lambda = 0$, 1 and 2. The free stream velocity is in the positive x-direction (approximately top left to bottom right) with the disk rotating clockwise from above. Semi-transparent grey isosurfaces are vorticity magnitude, $||\omega|| = 3$. Streamwise vorticity, ω_x (left column) and spanwise vorticity, ω_z (right column) are shown in opaque red and blue for positive (+3) and negative (−3) values, respectively. The x-, y- and z-axes reference lines are $5D$, $1D$ and $1D$ long, respectively.

indicating that the TSR value that leads to suppression of vortex shedding varies with the Reynolds number and angle of attack. At $\lambda = 2$, the flow is no longer steady and the advancing tip vortex continues to strengthen, resulting in a tail that persists further downstream. We also see another instability arise in the advancing tip vortex. The vortex core itself is displaced from its centre and begins to spiral around. The frequency of the spirals ($St = 0.10$) is approximately half that of the vortex-shedding instability at $\lambda = 0$ ($St = 0.17$). This swirling wake structure is remarkably similar to those seen for other axisymmetric spinning bluff bodies. Kim & Choi (2002) and Pier (2013) studied flow past a sphere rotating about its streamwise axis and found that rotation could strengthen one tip vortex over the other and induce a swirling wake for both steady and planar-symmetric shedding cases. In addition, Jiménez-González *et al.* (2014) observed similar swirling vortical structures in the flow past a spinning axisymmetric bullet-shaped body, where the oscillatory mode is deformed into a spiral by the body rotation. Jiménez-González *et al.* (2014) show that increasing rotation decreases the critical Reynolds number associated with this bifurcation to the oscillatory regime, allowing it to appear as rotation increases.

While further analysis into the swirling-wake instability is beyond the scope of the present work, we briefly comment on notable patterns between its appearance in these different configurations and remark on how these results may extend to similar cases. For the streamwise-rotating sphere, bullet-shaped body and rotating disk in normal flow ($\alpha = 90°$), the axisymmetry of the flow configurations allows the wake to align freely with the body (Kim & Choi 2002; Jiménez-González *et al.* 2014). In the case of the inclined disk ($\alpha < 90°$), the inclination automatically breaks the axisymmetry and creates

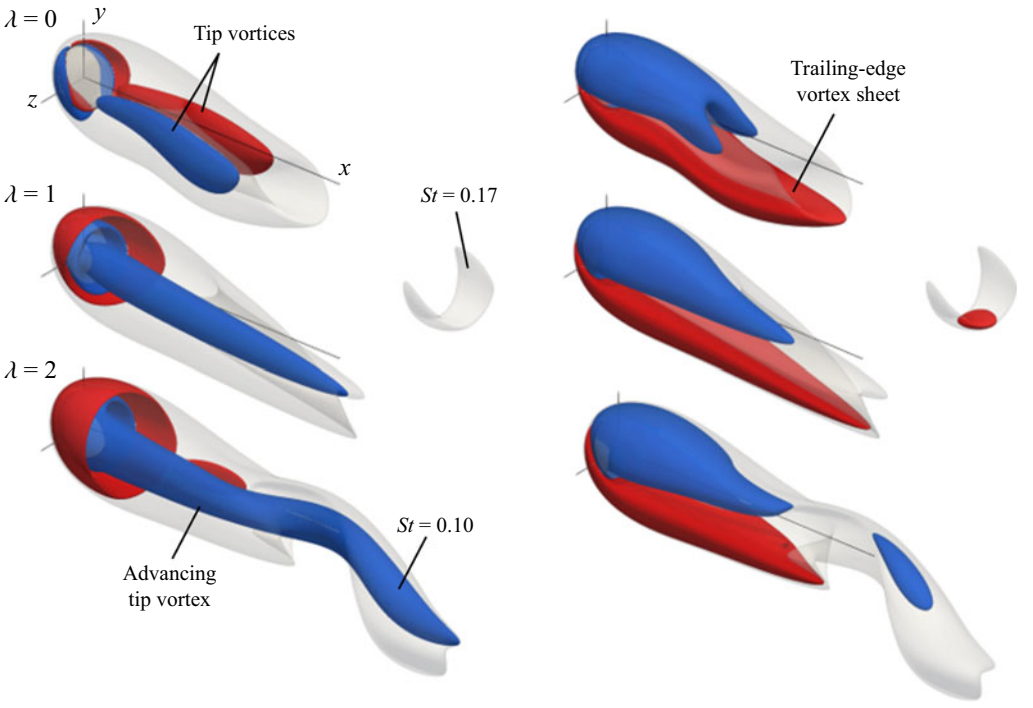

Figure 12. Isosurfaces of vorticity for the disk at $Re = 120$ and $\alpha = 60°$ for $\lambda = 0$, 1 and 2. The free stream velocity is in the positive x-direction (approximately top left to bottom right) with the disk rotating clockwise from above. Semi-transparent grey isosurfaces are vorticity magnitude, $||\omega|| = 0.8$. Streamwise vorticity, ω_x (left column) and spanwise vorticity, ω_z (right column) are shown in opaque red and blue for positive (+0.8) and negative (−0.8) values, respectively. The x-, y- and z-axes reference lines are $5D$, $1D$ and $1D$ long, respectively.

a spanwise, x–y-planar symmetry, causing the tip vortices to align spanwise along the z-axis. However, as $\alpha \to 90°$, the flow configuration approaches the axisymmetric case of the disk in normal flow and the selection of a particular plane of alignment for the tip vortices is less distinct. In these cases, the rotation may be strong enough to overcome the selection of an alignment plane, perturbing the flow into a spiral, as seen in the purely axisymmetric flow configurations. We propose that this swirling instability occurs when the body's rotation is above a critical value that overcomes the body configuration's wake alignment. This critical value will be lower as the flow configuration shows increasing axisymmetry about the free stream axis.

The vortex-shedding bifurcation is only the first in a series of bifurcations that take the flow from steady to chaotic flow. Characterising the effect of spin beyond the single-frequency periodic vortex-shedding regime will be important for understanding how the effect of spin extends to much higher Reynolds numbers, which are supercritical with respect to this array of bifurcations. While we do not study all of the different regimes, we briefly consider the case at $Re = 300$ and $\alpha = 50°$, which has undergone a second bifurcation at approximately $Re = 268$ and exhibits periodic shedding with low-frequency modulation (PSL) for the non-spinning case (Tian *et al.* 2017). Tian *et al.* (2017) showed that this modulation is associated with a low-frequency increase and decrease in the size of the recirculation bubble, which modulates the strength of the shed vortices. Figure 13 shows the modification to the wake for $Re = 300$ and $\alpha = 50°$ as TSR increases from zero to two. As with the $Re = 500$ and $\alpha = 25°$ case, we see hairpin vortices shed from the disk,

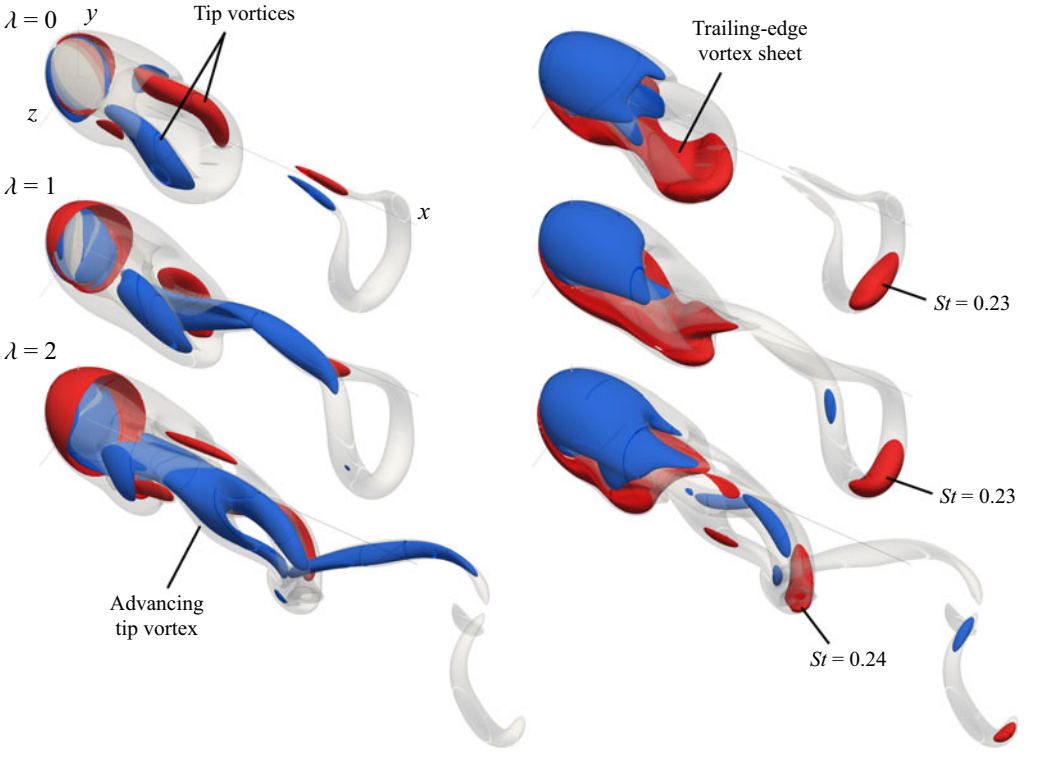

Figure 13. Isosurfaces of vorticity for the disk at $Re = 300$ and $\alpha = 50°$ for $\lambda = 0$, 1 and 2. The free stream velocity is in the positive x-direction (approximately top left to bottom right) with the disk rotating clockwise from above. Semi-transparent grey isosurfaces are vorticity magnitude, $||\omega|| = 3$. Streamwise vorticity, ω_x (left column) and spanwise vorticity, ω_z (right column) are shown in opaque red and blue for positive (+3) and negative (−3) values, respectively. In all three cases, the low-frequency modulation occurs at $St = 0.03$.

although the tip vortices are comparatively closer together and weaker as they peel away with the trailing-edge vortex sheet. Since the legs are weak, the hairpin vortices gradually form vortex loops as they convect downstream, similar to observations by Kim (2009). The additional low-frequency modulation appears as a gradual strengthening and weakening of the vorticity in the hairpin vortices.

As TSR increases from zero to two, spanwise planar symmetry breaks and the advancing tip vortex dominates. The frequency of the flow phenomena appears to be relatively independent of tip-speed ratio in this range. The frequency of periodic vortex shedding remains relatively constant at approximately $St = 0.23 - 0.24$, while the low-frequency modulation occurs at $St = 0.03$ in each case. At $\lambda = 2$, we also see a rotation of the planar alignment of the shedding, with the hairpin vortices orienting towards the advancing side of the disk rather than the trailing edge. This may arise because at higher angles of attack approaching normal flow, the selection of a plane for alignment of vortex shedding is less distinct compared with low angles of attack. In other words, for high angles of attack, the separation profile between spanwise sides is increasingly similar to that for the leading and trailing edges. In these cases, rotation can shift the alignment of vortex shedding. The low-frequency modulations are also less intense and the amplitude of shedding remains relatively constant in time, rather than strengthening and weakening as for $\lambda = 0$. In PSL flow, the spin does not lead to vortex-shedding suppression for TSRs up to two, but it does appear to have a stabilising effect on the low-frequency modulations.

Since decreased low-frequency modulation is observed, this suggests that the recirculation region undergoes smaller fluctuations in size as well.

5. Conclusions and discussion

The flow over a spinning disk at angle of attack was investigated at low Reynolds numbers where the first bifurcations occur and over values of tip-speed ratio (TSR) up to three. Spin introduced new bifurcations associated with instabilities that alter the aerodynamic forces and wake dynamics.

For flow over the spinning disk at $Re = 500$ and $\alpha = 25°$, increasing TSR causes a monotonic increase in lift and drag coefficients for tip-speed ratios up to three. This effect appears to be largely Reynolds number independent, with studies at $Re = O(10^5)$ showing increases of similar magnitude in lift and drag coefficients for $\lambda > 1$, though changes are negligible for $\lambda < 1$ (Potts 2005). Studies of Frisbee-like spinning disks (with rims and camber) at $Re = O(10^5)$ for TSRs up to one indicate negligible effect on lift and drag (Stilley & Carstens 1972; Potts & Crowther 2001). However, studies at higher tip speed ratios around two to three begin to show substantial increases in lift and drag, as well as increased circulation and downwash (Nakamura & Fukamachi 1991; Higuchi *et al.* 2000; Potts 2005), similar to trends observed in the present work. This suggests that for sufficiently high TSR ($\lambda \gtrapprox 1$), increasing lift and drag due to spin could be a Reynolds-number-independent effect, at least for $O(10^2) < Re < O(10^5)$.

We also observe several interesting phenomena, including the suppression of vortex shedding at moderate TSRs and the short-wavelength corkscrew-shaped $(-2, 0, 1)$ principal mode from the family of elliptic instabilities at higher TSRs. As λ increases, more vorticity is generated at the disk surface and ultimately advected into the wake. By analysing the pattern of streamlines in the wake, we show that the disk rotation produces a cone-shaped recirculation region that orients itself into the advancing tip vortex. As a result, vorticity generated from the suction side of the disk surface strengthens the advancing tip vortex. Meanwhile, vorticity generated from the pressure side of the disk is distributed across both the receding tip vortex and the trailing-edge vortex. The strengthened tip vortices induce a spanwise stretching of the trailing-edge vortex sheet as they entrain it. This serves to dissipate vorticity from the trailing-edge vortex sheet, preventing it from rolling up and resulting in weakened or suppressed vortex shedding.

At higher TSRs, the vortex-shedding instability reappears, which may be caused by the disk rotation strengthening the trailing-edge vortex sheet beyond the ability of the tip vortices to dissipate it. Overall, disk rotation causes two competing effects: (i) the increase in vorticity in the tip vortices, especially the advancing tip vortex, which helps to dissipate the trailing-edge vortex sheet; and (ii) the addition of vorticity into the trailing-edge vortex sheet. We hypothesise that the stronger of the two effects determines whether or not vortex shedding occurs. Further study quantifying the convection of vorticity generated by the rotating disk into the tip vortices and trailing-edge vortex sheet could help illuminate the exact mechanism of this non-monotonic suppression and subsequent destabilisation with increasing spin.

Vortex-shedding suppression is also observed in the additional cases explored in § 4. We conjecture that the stabilising effect of disk rotation may extend more broadly to the (Re, α) parameter space, particularly in the vortex-shedding flow regime near the bifurcation point. However, a more comprehensive parameter study would be required to assess the limits of this claim. The suppression of vortex shedding by rotation was also observed by Ouyang *et al.* (2022) for normal flow over a disk ($\chi = 50$) for a range of cases, including for $Re = 150$ at $0.5 \leq \lambda \leq 1.67$ and for $Re = 175$ at $1.0 \leq \lambda \leq 1.43$, studied,

though higher λ values were not explored. As Re increases, a higher λ is needed to suppress vortex shedding. Due to the streamwise rotational symmetry in their configuration, the wake also develops a 'frozen wake' in which the vortical structure in the wake swirls about the centre line, but appears frozen in the rotating body-fixed reference frame. The 'frozen wake' was coined by Kim & Choi (2002) who first observed the phenomenon for flow over a streamwise-rotating sphere. Due to the break in streamwise rotational symmetry when the disk is inclined to the flow, this 'frozen' wake is not observed or expected in the present study. Several scholars corroborate that moderate rotation rates can suppress or have a stabilising effect on vortex shedding for a variety of other rotating, axisymmetric, bluff-body configurations with a range of rotation axes from streamwise to spanwise, including for the rotating sphere (Kim & Choi 2002; Pregnalato, Thompson & Hourigan 2002; Giacobello 2005; Kim 2009; Poon *et al.* 2010; Pier 2013; Wang *et al.* 2016), the spinning cylinder (Kang, Choi & Lee 1999; Mittal & Kumar 2003; Karabelas *et al.* 2012; Pierson *et al.* 2019) and the spinning bullet-shaped body (Jiménez-González *et al.* 2014). This collection of studies suggests an overarching trend in the effect of rotation for bluff-body flow, where rotation introduces vorticity into the flow, strengthening vortical structures and significantly altering instability regimes. Given similarities in the trends and wake structures, it is possible that the underlying mechanisms in these various flows may be related as well, with strengthened vortices helping to dissipate vorticity in the shedding vortex sheets.

At high TSRs ($\lambda \geq 1.9$) beyond the region of vortex-shedding suppression, a distinct, short-wavelength instability appears, closely resembling the $(-2, 0, 1)$ principal mode associated with elliptical instability. By using SPOD to isolate this mode shape for $\lambda = 2$ and modelling the tip-vortices as Batchelor vortices, we are able to estimate the circulation Reynolds number, $Re_\Gamma = \Gamma/(2\pi\nu)$, and strain rate, ε, where Γ is the circulation and ν is the kinematic viscosity. These estimated values compare well with values required for instability in Batchelor vortices by Lacaze *et al.* (2007), despite the current axial velocity strength, W_0, exceeding those considered in their stability analysis. We also find that the frequency, wavenumbers and axial velocity strength satisfy the necessary conditions for perfect resonance of the $(-2, 0, 1)$ principal mode. For $(1.9 \leq \lambda \leq 2.2)$, we observe a lock-in phenomenon between the short-wavelength instability frequency and twice the disk rotation frequency, suggesting that the rotation acts as an additional forcing that helps to enhance the resonance of the elliptic instability, especially for this region where the flow is potentially close to the critical point (Lacaze *et al.* 2007). We also observe a range of TSRs right after the lock-in region $(2.3 \leq \lambda \leq 2.6)$ for which the energy of the elliptic instability first declines. The strength of the $(-2, 0, 1)$ mode may be enhanced specifically in this lock-in region thanks to resonance with the disk rotation forcing, allowing it to appear distinctly within this range, even though it is less apparent just beyond the lock-in range. For $2.6 \leq \lambda \leq 3$, the energy of the $(-2, 0, 1)$ mode continues to grow. This is consistent with the increasing growth rates of the mode as Re_Γ and ε increase with increasing λ. Given the unique circumstances under which this elliptic instability mode appears and the rarity of its observation in tip vortices of bluff-body wakes, we refrain from claiming that such instabilities would commonly arise in tip vortices stemming from bluff-body flow configurations. While our results highlight a significant and well-defined case where the instability can be realised, their broader occurrence likely depends on whether similarly specific conditions are met.

For the highest TSRs considered $(2.3 \leq \lambda \leq 3)$, the wake exhibits a nonlinear combination of vortex shedding and short-wavelength instability. At certain TSRs, such as for $2.6 \leq \lambda \leq 3$, the frequency peaks of these combined phenomena organise into harmonics of one another, with the SPOD modes revealing that hairpin-vortex shedding

occurs quasi-periodically with the braids of the elliptic instability. Vortex shedding occurs as a result of growing perturbations in the wake for a sufficiently strong trailing-edge vortex sheet. However, the $(-2, 0, 1)$ principal mode arises when resonance conditions are achieved with sufficient circulation, axial velocity and strain in the advancing tip vortex. While these instabilities arise by different mechanisms and are located in different parts of the wake, their proximity and similar structures allow them to interact when they are both present. Increasing TSR, in contrast to Re or α, is able to significantly modify the axial-velocity strength in the advancing tip vortex, as a result of the upstream flow generated by the recirculation region that injects linear momentum directly into the advancing tip vortex, Thus, spin can cause appropriate values of Re_Γ, ε and W_0 for the elliptic instability to arise. A broader study quantifying this effect would provide for a more accurate prediction of when the conditions for elliptic instability are met.

While there is a strong match with features from studies of the $(-2, 0, 1)$ principal mode in Batchelor vortices, some of the discrepancies in the non-idealised flow configuration will likely affect the prediction of the exact critical points as well. In addition to the discrepancy between the actual tip-vortex profile compared with the idealised Batchelor vortex shape, there is also the presence of the trailing-edge vortex sheet just outside the vortex core and other perturbations in the wake from the spinning disk. The vortex sheet may impose a significant strain on the tip vortex, as it does possess opposite streamwise vorticity to the advancing tip vortex and may affect estimates of the strain parameter, ε. Despite these discrepancies in the flow configuration, the strong match in mode shapes shows the robustness of these modes over a range of frequencies, wavenumbers and axial-velocity strength, as long as resonance conditions are met. Therefore, while we have considered here only a single (Re, α) combination, we expect these principal modes to emerge for a range of flow parameters if there is sufficient spin to produce the required flow profile in the tip vortices. Similarly, the frequency-lock-in effect between the disk rotation and the elliptic instability, as well as between vortex shedding and the elliptic instability in the mixed wake, is a condition-specific phenomenon that will arise when frequencies align appropriately.

While the observations in this study were made for low-Reynolds-number flow ($O(10^2)$) over a disk, there are some similarities with observations for high Reynolds number and for other bluff-body geometries. Kuraan & Savaş (2024) reported that the dominant vortex shedding frequency is only a weak function of tip-speed ratio and that it decreases with increasing angle of attack, both trends that are observed in the present low-Reynolds-number study. Within the limited range of overlapping angles of attack, Kuraan & Savaş (2024) found dominant shedding frequencies of $St = 0.35$ at $\alpha = 54°$ and $St = 0.24$ at $\alpha = 60°$. In comparison, the present study finds $St = 0.23$ at $\alpha = 50°$ and $Re = 300$, and $St = 0.17$ at $\alpha = 60°$ and $Re = 120$, which follow the same trend and are of similar order, though lower in magnitude and with the caveat of comparing across different Reynolds numbers. The structure of vortex-shedding instabilities observed at low Reynolds numbers has been shown to persist statistically as large-scale coherent structures at turbulent Reynolds numbers, for example, in flow over the inclined disk for up to $Re = 5 \times 10^4$ (Calvert 1967) and flow over an axisymmetric bluff body for up to $Re = 2 \times 10^5$ (Rigas *et al.* 2014). However, it remains to be seen if elliptic instabilities will continue to persist in bluff-body flow as Reynolds number increases into turbulent regimes. Although separation profiles and boundary layer formation are different for high Reynolds numbers, disk rotation inevitably injects both linear and angular momentum into the wake. Therefore, while we require further investigation at high Reynolds number to draw definitive conclusions, we speculate that the mechanisms uncovered here may offer some insight into the underlying flow physics for flow over different rotating bodies at high Reynolds number.

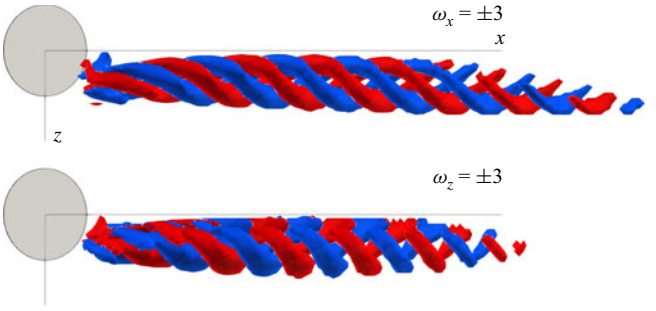

Figure 14. Top view of streamwise (top) and spanwise (bottom) vorticity isosurfaces of the most energetic SPOD mode for $Re = 500$, $\alpha = 25°$ and $\lambda = 2$, occurring with temporal frequency $\omega = 1.31$ and axial wavenumber $k = 1.9$.

Acknowledgements. The simulations presented in this work used the Extreme Science and Engineering Discovery Environment (XSEDE) Stampede 2 at the Texas Advanced Computing Center through allocation TG-CTS 120005. XSEDE is supported by National Science Foundation grant number ACI-1548562 (Towns *et al.* 2014).

Funding. This research was supported in part by The Boeing Company through grant CT-BA-GTA-1.

Declaration of interests. The authors report no conflict of interest.

Appendix A. Short-wavelength instability in the advancing tip vortex

A.1. *Spectral proper orthogonal decomposition for identifying energetic modes*

To analyse the structure and frequency of the short-wavelength instability, we use spectral proper orthogonal decomposition (SPOD) to identify the most energetic mode associated with the short-wavelength instability at $\lambda = 2$ (Towne, Schmidt & Colonius 2018). Since many instances of the flow field are necessary for SPOD, it can be memory intensive, especially for 3-D flows. Specifically, we use a streaming SPOD algorithm developed by Schmidt & Towne (2019), which efficiently processes the flow-field snapshots one by one, and makes SPOD for the 3-D flow field viable. To reduce the data usage while maintaining flow characteristics, we also coarsen the flow field data by a factor of five in each spatial direction.

For $Re = 500$, $\alpha = 25°$ and $\lambda = 2$, the highest energy SPOD mode occurs at $St = 1.31$ (or $\omega = 1.31$) and is shown in figure 14. The mode is confined to the advancing-tip-vortex core and we clearly see the double-helical braiding of positive and negative vorticity. The first mode captures most of the structure of the full flow field, with other frequency peaks being over an order of magnitude weaker. The missing features that are associated with these lower energy modes are the shedding of vortical blobs from the leading edge vortex sheet (figure 6).

A.2. *Elliptic instability in a pair of counter-rotating Batchelor vortices*

To characterise the short-wavelength instability, we first note its close resemblance to the $(-2, 0, 1)$ principal mode of the elliptic instability . Elliptic instability occurs as a result of the amplification of Kelvin modes in a vortex core due to an external strain field, often from an adjacent vortex (Widnall, Bliss & Tsai 1974). For flow over a spinning disk, the advancing tip vortex is strained by the adjacent, counter-rotating tip vortex on the receding side of the disk.

The elliptical instability has been studied in a variety of vortex-pair configurations, including various vorticity profiles, both counter- and co-rotating vortex pairs, and with and without axial flow. The most unstable mode depends on these details and is summarised by Kerswell (2002) and Leweke, Le Dizès & Williamson (2016). In particular, the Batchelor vortex has both Gaussian axial vorticity and axial velocity profiles, and thus closely matches the velocity profile for a pair of tip vortices behind wings (Batchelor 1964). The associated elliptic instabilities have been investigated in detail experimentally by Roy *et al.* (2011), and numerically by Ryan & Sheard (2007) and Lacaze *et al.* (2007). The elliptic instability can also arise in pairs of vortices with unequal strength (Roy *et al.* 2011), as is the case for the present spinning disk flow, where the strengthened advancing tip vortex is strained by the adjacent, but weaker, counter-rotating tip vortex on the receding side of the disk.

For a single Batchelor vortex, the non-dimensionalised axial vorticity, $\omega_0(r)$, and axial velocity, $W(r)$, are given by

$$\omega_0(r) = 2\exp(-r^2) \quad \text{and} \tag{A1}$$

$$W(r) = W_0 \exp(-r^2), \tag{A2}$$

where r is the radial distance, $W_0 = 2\pi R_0 \xi/\Gamma$ is the axial velocity strength, Γ is the circulation, ξ is the dimensional axial velocity and R_0 is the vortex radius. Note that the axial velocity strength, W_0, can also be written in terms of the ratio of the maximum axial velocity to the maximum azimuthal velocity to the maximum $W_0 = (0.638 \max V)/(\max W)$, where V is the azimuthal velocity. The azimuthal velocity is non-dimensionalised by the angular velocity in the vortex $\Omega_0 = \Gamma/(2\pi R_0^2)$, and can be written as

$$V(r) = \frac{1}{r}(1 - \exp(-r^2)). \tag{A3}$$

For a Batchelor vortex with a strain field applied, the flow is parametrised by the circulation Reynolds number, $Re_\Gamma = \Gamma/(2\pi\nu)$, the axial velocity strength, W_0, and the strain rate imposed on the vortex, ε, where ν is the kinematic viscosity. Using a point-vortex approximation, the strain rate can be approximated by

$$\varepsilon \approx \frac{\Gamma}{2\pi b^2}, \tag{A4}$$

where b is the distance between the centres of the two vortices.

The elliptic instability arises from resonance of Kelvin modes in the vortex core. Kelvin modes are the linear normal perturbation modes in the core of a columnar vortex in the inviscid limit (Thomson 1880). For the Batchelor vortex, the Kelvin modes are given in cylindrical coordinates (r, θ, z) for the velocity field, $\boldsymbol{u}'$, and pressure field, p', by

$$\boldsymbol{u}' = \boldsymbol{u}_K(r) \exp(ikz + im\theta - i\omega t) \quad \text{and} \tag{A5}$$

$$p' = p_K(r) \exp(ikz + im\theta - i\omega t), \tag{A6}$$

where k is the axial wavenumber, m is the azimuthal wavenumber and ω is the temporal frequency (not to be confused with the vorticity vector, $\boldsymbol{\omega}$) (Thomson 1880; Lacaze *et al.* 2007). Individual Kelvin modes are all neutrally stable or damped (Ryan & Sheard 2007). However, the strain imposed by one vortex on the adjacent vortex causes a coupling of pairs of Kelvin modes. These pairs are referred to as principal modes and they are able to resonate in certain conditions, giving rise to the elliptic instability.

To achieve resonance, the pairs of modes must have matching temporal frequency and axial wavenumbers, and their azimuthal wavenumbers must differ by two (see Eloy & Le

Dizès 2001; Lacaze, Birbaud & Le Dizès 2005). This can be written as

$$\omega_1 = \omega_2, \quad k_1 = k_2, \quad m_1 = m_2 \pm 2, \tag{A7}$$

where the subscripts denote the first and second mode of the pair. The branch label, l, gives the number of zeros in the radial velocity along the radial direction. Typically, the most unstable configuration is for $l_1 = l_2 = l$. As a result, principal modes are referenced by their azimuthal wavenumbers, m_1 and m_2, and a branch label, l, as (m_1, m_2, l). The condition for perfect resonance is given by Eloy & Le Dizès (2001) as

$$\omega - kW_0 = \frac{m_1 + m_2}{2}, \tag{A8}$$

relating the wavenumbers and temporal frequency to the axial velocity strength.

Lacaze *et al.* (2007) performed a stability analysis to identify the most unstable principal modes in the pair of counter-rotating Batchelor vortices for a range of Re_Γ, W_0 and ε values. They find that the principal modes (m_1, m_2, l) of the elliptic instability are unstable for sufficiently high circulation Reynolds number and strain rate. The axial velocity strength, W_0, is the strongest factor in determining the most unstable principal modes. This is due to the presence or absence of a critical layer and its associated damping for the various Kelvin modes as W_0 changes. As a result, the amount of axial flow plays a key role in the nature of the elliptic instability. While the $(-1, 1, 1)$ principal mode is dominant for vortex pairs with no axial flow, this mode becomes damped in the presence of axial flow. Instead, the $(-2, 0, 1)$ principal mode is most unstable in flows with sufficient axial flow ($W_0 \geq 0.2$), where the critical-layer damping rate decreases in magnitude as W_0 increases (Lacaze *et al.* 2007). This $(-2, 0, 1)$ principal mode consists of the resonant coupling between the $m = 0$ Kelvin mode, which produces axial swelling and contracting of the vortex core, and the $m = -2$ Kelvin mode, which consists of the alternating braiding of positive and negative vorticity perturbations (Ryan & Sheard 2007). The $m = -1$ mode is strongly damped at low W_0, but is neutrally stable for $W_0 \geq 0.5$ (Lacaze *et al.* 2007). In combination, this results in a cork-screw vortical structure with an axial wavelength of the order of the inter-vortex distance. Comparing these vorticity isosurface representations, we see substantial qualitative match in the short-wavelength instability and the $(-2, 0, 1)$ principal mode shown by Leweke *et al.* (2016). They both feature a double-helical, corkscrew shape of the vortex core.

A.3. *Modelling tip vortices as a pair of counter-rotating Batchelor vortices*

To provide a quantitative comparison between the observed short-wavelength instability and the elliptic instability, we estimate the flow parameters in the advancing tip vortex that are relevant to the conditions that lead to elliptic instability. Specifically, we will examine the case of the disk at $Re = 500$, $\alpha = 25°$ and $\lambda = 2$, where the short-wavelength instability is observed distinctly. The relevant parameters are the axial velocity strength, W_0, the circulation Reynolds number, Re_Γ, and the strain rate, ε. These values can change along the length of the advancing tip vortex so we estimate the values at several streamwise distances to evaluate the range of values found in the vortex, and ultimately focus on the representative mid-wake at around $x/D = 6$. We start by modelling the mean flow in the tip vortices as a pair of counter-rotating Batchelor vortices. We use vortices with unequal strengths, since the advancing tip vortex is considerably stronger than the receding tip vortex. The mean flow is shown in figure 16. Note that the receding tip vortex is present, but weaker than the advancing tip vortex.

The axial velocity strength, W_0, scales with the ratio of maximum axial velocity to maximum azimuthal velocity. In the tip-vortex configuration, the non-zero axial velocity

Figure 15. Top view of streamwise vorticity isosurface ($\omega_x = 1$) for the mean flow at $Re = 500$, $\alpha = 25°$ and $\lambda = 2$.

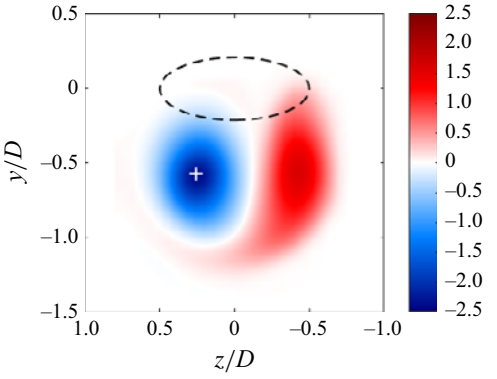

Figure 16. Cross-section of streamwise vorticity, ω_x, for the mean flow at $Re = 500$, $\alpha = 25°$ and $\lambda = 2$. The dashed ellipse denotes the streamwise-projected outline of the disk. The white cross marks the peak streamwise vorticity in the advancing tip vortex.

arises from the velocity deficit in the vortex cores, with axial velocity tending to the free stream velocity away from the vortex core. By changing to the free stream-fixed reference frame, this is equivalent to the general configuration outlined by the vortex profile in (A1), namely a peak axial velocity at the vortex centre that goes to zero with increasing radial distance. As TSR is increased, we saw that the rotation induces a recirculation region that aligns with the advancing tip vortex and creates a region of upstream flow. Overall, this increases the velocity deficit in the vortex cores, resulting in higher W_0 as TSR increases.

To determine the axial velocity strength, W_0, we determine the maximum azimuthal velocity and maximum axial velocity in the advancing tip vortex at a given streamwise plane. Note that the azimuthal velocity profile can be fit using either the maximum azimuthal velocity (A3) or using the maximum axial vorticity (A1). The maximum axial vorticity provides the centre of the vortices for estimating the inter-vortex distance b. Figure 17 provides an example fit for the Batchelor vortices based on fitting the Gaussian profiles to the maximum axial vorticity and maximum axial velocity. We include the resulting azimuthal velocity estimate to show that while this model provides a reasonable estimate, it does not fully capture the tip-vortex configuration. While a more involved optimisation could be performed, this crude approximation is quite reasonable given that the Batchelor vortex model is incomplete and will not be able to account for the presence of other vortical structures in the wake such as the leading-edge and trailing-edge vortex sheets.

The estimates of axial velocity strength using both azimuthal velocity estimates are shown in figure 18. There is some variability along the length of the vortex and between the two methods, with the value being in the range of $W_0 \approx 1.2-1.4$ at the mid-wake $x/D = 6$.

To determine the circulation Reynolds number, we estimate the total circulation in the advancing tip vortex by integrating the negative streamwise vorticity in the vortex for

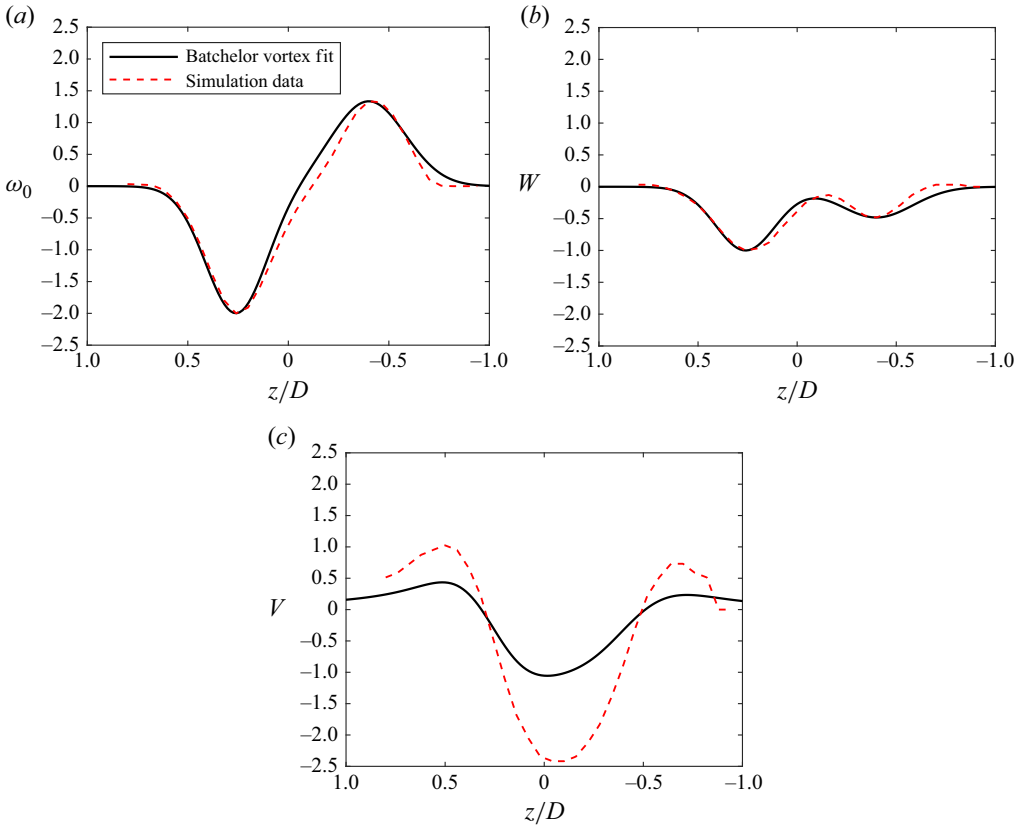

Figure 17. Comparison of the real profile and the modelled Batchelor vortex profiles along the spanwise line passing through the point of peak vorticity in the advancing tip vortex at $x/D = 6$, with peaks determined using max W and max ω_0 for (*a*) axial vorticity, (*b*) axial velocity and (*c*) azimuthal velocity. Flow profiles at other streamwise locations in the range of $2.5 \leq x/D \leq 10$ show a similar match and are omitted for clarity.

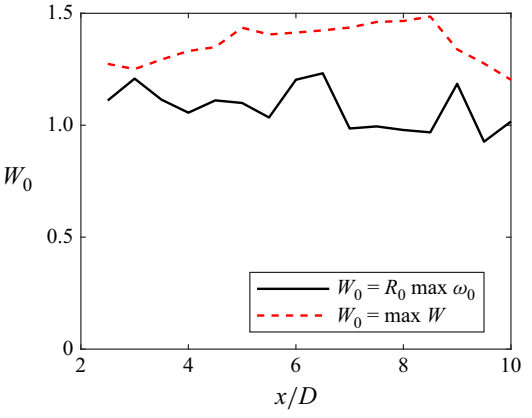

Figure 18. Axial velocity strength, W_0, with streamwise distance estimated from either fitting the Batchelor vortex profile to the maximum axial vorticity or the maximum axial velocity.

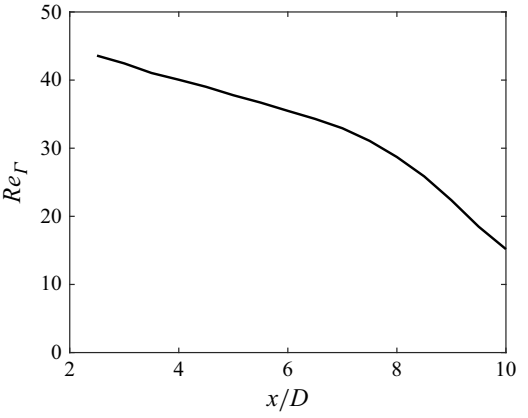

Figure 19. Circulation Reynolds number, Re_Γ, against streamwise distance.

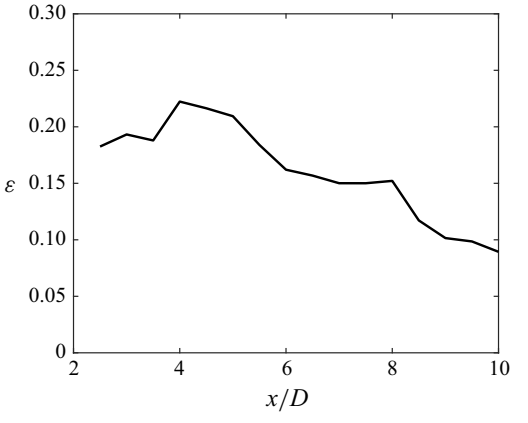

Figure 20. Strain rate estimate, $\varepsilon \approx \Gamma/(2\pi b^2)$, as a function of streamwise distance.

each streamwise plane. Figure 19 shows the variation in the circulation Reynolds number with streamwise distance. The circulation Reynolds number decreases as vorticity diffuses by viscous effects. We can estimate the circulation Reynolds number as $Re_\Gamma \approx 35$ in the mid-wake around $x/D = 6$.

The strain rate, ε, can be estimated for a known circulation, Γ, and inter-vortex distance, b, by (A4). Note that the circulation used is for the adjacent vortex, namely the receding tip vortex. The inter tip-vortex distance is determined by the distance between the peaks in axial velocity in both tip vortices. Figure 20 shows the strain rate estimate against streamwise distance. Strain decreases since it is dependent on the circulation, which decreases with downstream distance. We can estimate the strain as $\varepsilon \approx 0.15$ in the mid-wake at approximately $x/D = 6$.

Having estimated the parameters in the tip vortices using the Batchelor vortex model, we perform several different comparisons between the short-wavelength instability and the elliptic instability. Using the equation for perfect resonance (A8), we can use the wavenumbers and frequency of the short-wavelength SPOD mode (Appendix A.1) to calculate the axial velocity strength that would be required for the principal mode to be unstable. For the SPOD mode at $\lambda = 2$ with $St = 1.31$, $k = 1.9$, $m_1 = -2$ and $m_2 = 0$, (A8) predicts perfect resonance for an axial velocity strength of $W_0 = 1.22$. This matches

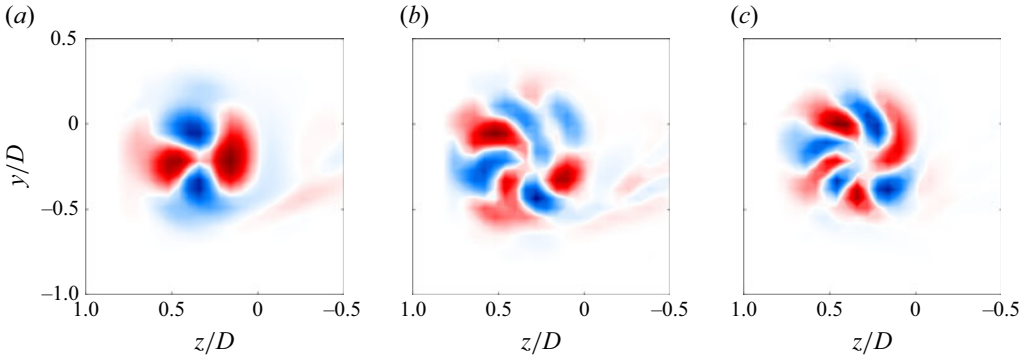

Figure 21. Streamwise vorticity in a streamwise cross-section ($x/D = 6$) of the SPOD modes at (*a*) $St = 1.31$ ($k = 1.9$ and $\omega = 1.31$), (*b*) $St = 2.06$ ($k = 3.0$ and $\omega = 2.06$) and (*c*) $St = 2.59$ ($k = 3.8$ and $\omega = 2.59$), for the disk at $Re = 500$, $\alpha = 25°$ and $\lambda = 2$. The vorticity contour levels for each mode are normalised by the peak value of that mode for clarity. The modes at $St = 2.06$ and $St = 2.59$ are significantly weaker, with energy-spectra peak magnitudes of 0.007 and 0.02, respectively, when normalised by the energy-spectra peak magnitude of the mode at $St = 1.31$.

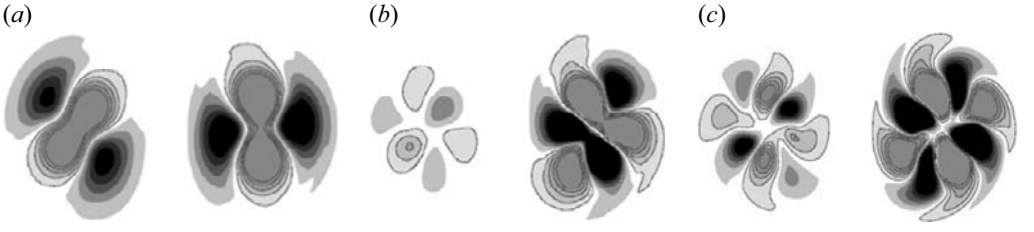

Figure 22. Cross-sections of the vorticity perturbation fields of principal modes: (*a*) $(-2, 0, 1)$ with $k = 1.88$; (*b*) $(-3, -1, 1)$ with $k = 3.23$; and (*c*) $(-4, -2, 1)$ with $k = 4.57$, from simulations at $W_0 = 0.482$, $Re = 3180$ and $\varepsilon = 0.063$ by Lacaze *et al.* (2007). Reproduced with permission from Lacaze *et al.* (2007, 357).

closely with the axial velocity strength estimate of $W_0 \approx 1.2-1.4$, indicating that the tip-vortex configuration supports perfect resonance of the $(-2, 0, 1)$ principal mode.

Figure 21 shows streamwise cross-sections of the SPOD modes for flow over the disk at $Re = 500$, $\alpha = 25°$ and $\lambda = 2$ for comparison with various elliptic-instability principal modes. Although principal modes can show resonance for a range of (k, ω) combinations depending on W_0 (by the resonance condition in (A8)), the mode shapes themselves maintain the same qualitative features. As a result, while we do not have direct literature comparisons for our estimated vortex configuration $Re_\Gamma \approx 35$ and $\varepsilon \approx 0.15$, we can still find strong qualitative comparisons across different (Re_Γ, ε) values. We compare with the $(-2, 0, 1)$, $(-3, -1, 1)$ and $(-4, -2, 1)$ principal modes presented by Lacaze *et al.* (2007) for $W_0 = 0.482$, $Re = 3180$ and $\varepsilon = 0.063$, shown in figure 22. The SPOD mode at $St = 1.31$ displays the same structure as the $(-2, 0, 1)$ principal mode, with four lobes of alternating vorticity sign arranged in a circle (figure 22). The same is true comparing the SPOD modes at $St = 2.06$ and $St = 2.59$ with the $(-3, -1, 1)$ and $(-4, -2, 1)$ principal modes, respectively, but featuring six and eight lobes, respectively. Note that while the energies of the SPOD modes at $St = 2.06$ and $St = 2.59$ are approximately three orders of magnitude lower than that of the most energetic SPOD mode at $St = 1.3$, they form distinct peaks above the noise level. The axial velocity strength required for the perfect resonance of these SPOD modes at $St = 2.06$ and $St = 2.59$ are $W_0 \approx 1.4$ and $W_0 \approx 1.5$, respectively. These are in line with the estimate of $W_0 \approx 1.2-1.4$, although the estimate is

too crude to state for certain the level of resonance achieved. This matches with the analysis by Lacaze *et al.* (2007), which shows that for $W_0 \geq 0.5$, the $(-2, 0, 1)$ principal mode is more unstable than both the $(-3, -1, 1)$ and $(-4, -2, 1)$ principal modes. Regardless, we draw attention to them because they are still present with very low spectral energy, indicating that they may be neutrally stable or weakly damped.

Lacaze *et al.* (2007) show the most unstable modes in the $(W_0, \varepsilon Re_\Gamma)$ parameter space. For $\varepsilon = 0.1$ within the range $0 \leq W_0 \leq 0.6$, all of the principal modes are stable at least up to $\varepsilon Re_\Gamma \approx 4$. Increasing strain rate lowers the Reynolds number at which the modes first become unstable, since strain amplifies the resonance of the modes. The most unstable principal mode at $Re_\Gamma = O(10)$ for $W_0 \geq 0.18$ is the $(-2, 0, 1)$ mode (Lacaze *et al.* 2007). The lowest Re_Γ at which the mode is unstable depends on W_0, but is as low as $\varepsilon Re_\Gamma \approx 4$ at $W_0 = 0.4$. Since Lacaze *et al.* (2007) only consider $W_0 \leq 0.6$, it is not possible to make a direct comparison. However, we could reasonably expect the $(-2, 0, 1)$ principal mode to continue to show resonant properties, since the individual Kelvin modes are neutrally stable for $W_0 \geq 0.5$ (Lacaze *et al.* 2007). Based on our estimates, the tip vortices have $\varepsilon Re_\Gamma \approx 5$ with $W_0 \approx 1.2{-}1.4$. Therefore, the advancing tip vortex for $Re = 500$, $\alpha = 25°$ and $\lambda = 2$ does possess the correct order of magnitude of flow parameters for the $(-2, 0, 1)$ mode to be unstable, when modelled as a Batchelor vortex pair. This is consistent with the onset of the elliptic instability at approximately $\lambda = 1.8$, where the circulation Reynolds number and strain will be slightly lower than for the $\lambda = 2$ case since the advancing tip vortex is weaker. For the highest axial velocity strength considered by Lacaze *et al.* (2007), the axial wavenumber of the flow is $k \approx 2$ and is fairly independent of W_0, Re_Γ and ε for $W_0 > 0.5$. This matches well with the axial wavenumber of the short-wavelength SPOD mode at approximately $k = 1.9$. In summary, based on the qualitative and quantitative match described in this appendix, we conclude that the short-wavelength instability observed for flow over the disk at $Re = 500$, $\alpha = 25°$ and $\lambda = 1.5$, is the $(-2, 0, 1)$ principal mode of the elliptic instability.

References

Auguste, F., Fabre, D. & Magnaudet, J. 2010 Bifurcations in the wake of a thick circular disk. *Theor. Comput. Fluid Dyn.* **24** (1-4), 305–313.

Batchelor, G.K. 1964 Axial flow in trailing line vortices. *J. Fluid Mech.* **20** (4), 645–658.

Calvert, J.R. 1967 Experiments on the flow past an inclined disk. *J. Fluid Mech.* **29** (4), 691–703.

Chrust, M., Bouchet, G. & Dusek, J. 2010 Parametric study of the transition in the wake of oblate spheroids and flat cylinders. *J. Fluid Mech.* **665**, 199.

Chrust, M., Dauteuille, C., Bobinski, T., Rokicki, J., Goujon-Durand, S., Wesfreid, J.E., Bouchet, G. & Dušek, J. 2015 Effect of inclination on the transition scenario in the wake of fixed disks and flat cylinders. *J. Fluid Mech.* **770**, 189–209.

Eloy, C. & Le Dizès, S. 2001 Stability of the Rankine vortex in a multipolar strain field. *Phys. Fluids* **13** (3), 660–676.

Gao, S., Tao, L., Tian, X. & Yang, J. 2018 Flow around an inclined circular disk. *J. Fluid Mech.* **851**, 687–714.

Ghaddar, N.K., Korczak, K.Z., Mikic, B.B. & Patera, A.T. 1986 Numerical investigation of incompressible flow in grooved channels. Part 1. Stability and self-sustained oscillations. *J. Fluid Mech.* **163**, 99–127.

Giacobello, M. 2005 Wake structure of a transversely rotating sphere at moderate reynolds numbers. PhD thesis, University of Melbourne, Department of Mechanical and Manufacturing Engineering, Melbourne, Australia.

Goza, A. & Colonius, T. 2017 A strongly-coupled immersed-boundary formulation for thin elastic structures. *J. Comput. Phys.* **336**, 401–411.

Higuchi, H., Goto, Y., Hiramoto, R. & Meisel, I. 2000 Rotating flying disks and formation of trailing vortices. In *18th AIAA Applied Aerodynamics Conference*, pp. 4001. American Institute of Aeronautics and Astronautics.

Jiménez-González, J.I., Sevilla, A., Sanmiguel-Rojas, E. & Martínez-Bazán, C. 2014 Global stability analysis of the axisymmetric wake past a spinning bullet-shaped body. *J. Fluid Mech.* **748**, 302–327.

Kallemov, B., Bhalla, A., Griffith, B. & Donev, A. 2016 An immersed boundary method for rigid bodies. *Commun. Appl. Maths Comput. Sci.* **11** (1), 79–141.

Kang, S., Choi, H. & Lee, S. 1999 Laminar flow past a rotating circular cylinder. *Phys. Fluids* **11** (11), 3312–3321.

Karabelas, S.J., Koumroglou, B.C., Argyropoulos, C.D. & Markatos, N.C. 2012 High Reynolds number turbulent flow past a rotating cylinder. *Appl. Math. Model.* **36** (1), 379–398.

Kerswell, R.R. 2002 Elliptical instability. *Annu. Rev. Fluid Mech.* **34** (1), 83–113.

Kim, D. 2009 Laminar flow past a sphere rotating in the transverse direction. *J. Mech. Sci. Technol.* **23** (2), 578–589.

Kim, D. & Choi, H. 2002 Laminar flow past a sphere rotating in the streamwise direction. *J. Fluid Mech.* **461**, 365–386.

Kuraan, A.M. & Savaş, Ö. 2024 Flows over a spinning disc at incidence. *J. Fluid Mech.* **999**, A95.

Lacaze, L., Birbaud, A.-L. & Le Dizès, S. 2005 Elliptic instability in a rankine vortex with axial flow. *Phys. Fluids* **17** (1), 017101–017101.

Lacaze, L., Ryan, K. & Le Dizès, S. 2007 Elliptic instability in a strained batchelor vortex. *J. Fluid Mech.* **577**, 341–361.

Leweke, T., Le Dizès, S. & Williamson, C.H.K. 2016 Dynamics and instabilities of vortex Pairs. *Annu. Rev. Fluid Mech.* **48**, 507–541.

Liska, S. & Colonius, T. 2014 A parallel fast multipole method for elliptic difference equations. *J. Comput. Phys.* **278**, 76–91.

Liska, S. & Colonius, T. 2016 A fast lattice Green's function method for solving viscous incompressible flows on unbounded domains. *J. Comput. Phys.* **316**, 360–384.

Liska, S. & Colonius, T. 2017 A fast immersed boundary method for external incompressible viscous flows using lattice Green's functions. *J. Comput. Phys.* **331**, 257–279.

Lorenz, R.D. 2007 *Spinning Flight: Dynamics of Frisbees, Boomerangs, Samaras, and Skipping Stones*. Springer Science & Business Media.

Meliga, P., Chomaz, J.-M. & Sipp, D. 2009 Global mode interaction and pattern selection in the wake of a disk: a weakly nonlinear expansion. *J. Fluid Mech.* **633**, 159–189.

Mittal, S. & Kumar, B. 2003 Flow past a rotating cylinder. *J. Fluid Mech.* **476**, 303–334.

Munday, P.M. & Taira, K. 2018 Effects of wall-normal and angular momentum injections in airfoil separation control. *AIAA J.* **56** (5), 1830–1842.

Nakamura, Y. & Fukamachi, N. 1991 Visualization of the flow past a frisbee. *Fluid Dyn. Res.* **7** (1), 31.

Olivucci, P., Ricco, P. & Aghdam, S.K. 2019 Turbulent drag reduction by rotating rings and wall-distributed actuation. *Phys. Rev. Fluids* **4** (9), 093904.

Ouyang, D., Tian, X., Zhao, Y., Wen, B., Li, X., Li, J., Peng, T. & Peng, Z. 2022 Wake transitions behind a streamwise rotating disk. *J. Fluid Mech.* **953**, A24.

Pereira, J.C.F. & Sousa, J.M.M. 1993 Finite volume calculations of self-sustained oscillations in a grooved channel. *J. Comput. Phys.* **106** (1), 19–29.

Persson, P.-O. & Strang, G. 2004 A simple mesh generator in matlab. *SIAM Rev.* **46** (2), 329–345.

Pier, B. 2013 Periodic and quasiperiodic vortex shedding in the wake of a rotating sphere. *J. Fluids Struct.* **41**, 43–50.

Pierson, J.-L., Auguste, F., Hammouti, A. & Wachs, A. 2019 Inertial flow past a finite-length axisymmetric cylinder of aspect ratio 3: effect of the yaw angle. *Phys. Rev. Fluids* **4** (4), 044802.

Pines, D.J. & Bohorquez, F. 2006 Challenges facing future micro-air-vehicle development. *J. Aircraft* **43** (2), 290–305.

Poon, E.K.W., Ooi, A.S.H., Giacobello, M. & Cohen, R.C.Z. 2010 Laminar flow structures from a rotating sphere: effect of rotating axis angle. *Intl J. Heat Fluid Flow* **31** (5), 961–972.

Potts, J. & Crowther, W. 2001 Flight control of a spin stabilised axi-symmetric disc-wing. In *39th AIAA Aerospace Sciences Meeting and Exhibit*, pp. 253. American Institute of Aeronautics and Astronautics.

Potts, J. & Crowther, W. 2002 Frisbee (tm) aerodynamics. In *20th AIAA Applied Aerodynamics Conference*, pp. 3150. American Institute of Aeronautics and Astronautics.

Potts, J.R. 2005 Disc-wing aerodynamics. PhD thesis, University of Manchester Manchester, Manchester, United Kingdom.

Pregnalato, C.J., Thompson, M.C. & Hourigan, K. 2002 Flow transitions in the wake of a streamwise-rotating sphere. In *Symposium on Bluff Body Wakes and Vortex-Induced Vibrations (BBVIV3)*. Monash University.

RICCO, P. & HAHN, S. 2013 Turbulent drag reduction through rotating discs. *J. Fluid Mech.* **722**, 267–290.
RIGAS, G., OXLADE, A.R., MORGANS, A.S. & MORRISON, J.F. 2014 Low-dimensional dynamics of a turbulent axisymmetric wake. *J. Fluid Mech.* **755**, R5.
ROMA, A.M., PESKIN, C.S. & BERGER, M.J. 1999 An adaptive version of the immersed boundary method. *J. Comput. Phys.* **153** (2), 509–534.
ROY, C., LEWEKE, T., THOMPSON, M.C. & HOURIGAN, K. 2011 Experiments on the elliptic instability in vortex pairs with axial core flow. *J. Fluid Mech.* **677**, 383–416.
RYAN, K. & SHEARD, G.J. 2007 Non-linear growth of short-wave instabilities in a batchelor vortex pair. In *16th Australasian Fluid Mechanics Conference*. School of Engineering, The University of Queensland.
SCHMIDT, O.T. & TOWNE, A. 2019 An efficient streaming algorithm for spectral proper orthogonal decomposition. *Comput. Phys. Commun.* **237**, 98–109.
STILLEY, G. & CARSTENS, D. 1972 Adaptation of the frisbee flight principle to delivery of special ordnance. In *2nd Atmospheric Flight Mechanics Conference*, pp. 982. American Institute of Aeronautics and Astronautics.
TAIRA, K. & COLONIUS, T. 2009 Three-dimensional flows around low-aspect-ratio flat-plate wings at low Reynolds numbers. *J. Fluid Mech.* **623**, 187–207.
TAIRA, K., DICKSON, W., COLONIUS, T., DICKINSON, M. & ROWLEY, C. 2007 Unsteadiness in flow over a flat plate at angle-of-attack at low Reynolds numbers. In *45th AIAA Aerospace Sciences Meeting and Exhibit*, pp. 710. American Institute of Aeronautics and Astronautics.
THOMSON, W. 1880 XXIV. Vibrations of a columnar vortex. *Lond. Edin. Dublin Phil. Mag. J. Sci.* **10** (61), 155–168.
TIAN, X., HU, Z., LU, H. & YANG, J. 2017 Direct numerical simulations on the flow past an inclined circular disk. *J. Fluids Struct.* **72**, 152–168.
TOWNE, A., SCHMIDT, O.T. & COLONIUS, T. 2018 Spectral proper orthogonal decomposition and its relationship to dynamic mode decomposition and resolvent analysis. *J. Fluid Mech.* **847**, 821–867.
TOWNS, J. *et al.* 2014 XSEDE: accelerating scientific discovery. *Comput. Sci. Engng* **16** (05), 62–74.
VON KÁRMÁN, T. 1921 Über laminare und turbulente Reibung. *ZAMM-J. Appl. Math Mechan./Z. Angew. Math. Mech.* **1** (4), 233–252.
WANG, Y., SHU, C., TEO, C.J. & YANG, L.M. 2016 An efficient immersed boundary-lattice Boltzmann flux solver for simulation of 3D incompressible flows with complex geometry. *Comput. Fluids* **124**, 54–66.
WIDNALL, S.E., BLISS, D.B. & TSAI, C.-Y. 1974 The instability of short waves on a vortex ring. *J. Fluid Mech.* **66** (1), 35–47.
YANG, X., ZHANG, X., LI, Z. & HE, G.-W. 2009 A smoothing technique for discrete delta functions with application to immersed boundary method in moving boundary simulations. *J. Comput. Phys.* **228** (20), 7821–7836.